Mineralium Deposita (2023) 58:1537–1558
https://doi.org/10.1007/s00126-023-01191-x

ARTICLE

Mineralogy and trace element geochemistry of hydrothermal sulfides from the Ari vent field, Central Indian Ridge

Sun Ki Choi[1] · Sang Joon Pak[1,2] · Jonguk Kim[1] · Ji Young Shin[3] · Seungjin Yang[1] · Hwimin Jang[4] · Seung-Kyu Son[1]

Received: 24 May 2022 / Accepted: 26 June 2023 / Published online: 22 July 2023

Abstract

The Ari vent field (AVF) is an ultramafic-hosted seafloor massive sulfide (SMS) deposit in the middle part of the Central Indian Ridge. In this paper, we describe the detailed mineralogy and geochemistry of hydrothermal sulfide samples from the AVF, which can be classified into Fe–Cu- and Cu-rich types based on the major sulfide minerals. Sulfide mineralisation of the former type comprises: (1) stage I, early deposition of magnetite, pyrrhotite, isocubanite, chalcopyrite, and subhedral–euhedral pyrite under high-temperature fluid conditions (> 335 °C); (2) stage II, deposition of colloform pyrite, sphalerite, galena, and electrum from low-temperature fluids (< 200 °C) during the later mineralisation stage; and (3) stage III, seawater alteration that caused the precipitation of uraninite and chalcocite. This indicates that the fluids in the AVF had decreasing temperature and fS_2 and increasing fO_2 as mineralisation proceeded. The Cu-rich sulfide samples have mineral assemblages and a paragenesis similar to those of the Fe–Cu-rich sulfide samples, but the higher proportion of isocubanite is indicative of relatively high-temperatures and reducing conditions during mineralisation. Bulk chemical compositions of the AVF sulfides are characterised by high U contents (up to 51.9 ppm) and a distinct Sn distribution (2.1–86.4 ppm) between the two different types of hydrothermal samples, which differ from those of other ultramafic-hosted sulfide deposits. The U content is controlled mainly by the precipitation of discrete uraninite grains (< 1 μm in size) on altered surfaces of pyrite and hematite. The oxidative alteration of Fe-bearing minerals caused the fixation of seawater-derived U. Laser ablation–inductively coupled plasma–mass spectrometry analysis showed that most trace elements occur in solid solution in the sulfide minerals, mainly controlled by the physicochemical conditions of the hydrothermal fluids (e.g. temperature, fS_2, and fO_2). In particular, a comparative analysis of other mid-ocean ridge systems shows that the ultramafic-hosted sphalerite and pyrite are more enriched in Sn as compared with those hosted by basaltic rocks. However, the Fe–Cu-rich sulfide samples of the AVF are Sn-poor (< 10.2 ppm), because pyrite is substantially depleted in Sn (mostly < 1 ppm) as compared with sphalerite, regardless of the effect of the ultramafic-hosted mineralisation. This indicates that in situ trace element analysis of sphalerite and pyrite, especially for Sn, can provide insights into the different hydrothermal mineralisation in basaltic- and ultramafic-hosted systems, which cannot necessarily be inferred from bulk analysis. Our comparison also suggests that the Sn contents of ultramafic-hosted SMS deposits would be a possible source of Sn for the ultramafic-hosted volcanogenic massive sulfide (UM-VMS) deposit. The $\delta^{34}S$ values (+ 6.2 to + 8.5‰) of the pyrite record thermochemical sulfate reduction of seawater, which suggests that sulfur and most metals were predominantly leached from the associated host rocks with a contribution (29–40%) from reduced seawater sulfur. In conclusion, the AVF is a rock-dominated system that contains ultramafic-hosted mineralisation in the Central Indian Ridge.

Keywords Ultramafic-hosted hydrothermal mineralisation · Uranium · Tin · Ari vent field · Central Indian Ridge

Introduction

Mineralogical and geochemical features of seafloor massive sulfide (SMS) deposits at mid-ocean ridge (MOR) spreading centres vary significantly due to the different types of ridge (i.e., fast versus slow spreading) (Hannington

Editorial handling: A. R. Cabral

✉ Sang Joon Pak
electrum@kigam.re.kr

Extended author information available on the last page of the article

et al. 2005; Fouquet et al. 2010). At fast-spreading ridges, hydrothermal fluids only circulate in the upper part of oceanic crust at depths of 1–2 km, which is a region that comprises MOR basalt (MORB) and sheeted dyke, due to the presence of shallow magma chambers (Hannington et al. 2005). In contrast, at slow- to intermediate-spreading ridges, deep-rooted, large-offset detachment faults play an important role in causing amagmatic extension, which allows hydrothermal circulation to occur at much greater depths (~ up to 7 km) and enables fluid interaction with more ultramafic lithologies as compared with fast-spreading systems (McCaig et al. 2007; Escartín et al. 2008). These differences affect the redox state and metal contents of hydrothermal fluids, thereby producing different sulfide mineralogies and contrasts in geochemistry of SMS deposits in MORB- and ultramafic-hosted systems (Hannington et al. 2005; Fouquet et al. 2010; Patten et al. 2016; Knight et al. 2018; Fuchs et al. 2019). Ultramafic-hosted SMS deposits are typically characterised by reduced sulfide assemblages (pyrrhotite–isocubanite–chalcopyrite–Fe-rich sphalerite) and high Cu, Zn, Co, Au, Sn, and Ni contents relative to those of MORB-hosted SMS deposits (Hannington et al. 2005; Fouquet et al. 2010).

Numerous SMS deposits have been discovered along MOR settings since the first discovery of a seafloor hydrothermal venting site at the Galapagos Rift in 1977 (Corliss et al. 1979; Hannington et al. 2011). Although studies have been conducted on the mineralogy and geochemistry of SMS deposits along the Mid-Atlantic Ridge (Marques et al. 2006; Fouquet et al. 2010; Melekestseva et al. 2014; Ren et al. 2021), relatively little is known about SMS deposits in the Central Indian Ridge (CIR). In particular, few studies of the CIR have investigated the hydrothermal processes and genetic environments associated with ultramafic-hosted SMS deposits, such as the Kairei and Cheoeum vent fields (Wang et al. 2014, 2018; Choi et al. 2021). As such, further studies are required to obtain a better understanding of ultramafic-hosted hydrothermal mineralisation in the CIR.

Since 2009, the Korea Institute of Ocean Science and Technology (KIOST) has conducted hydrothermal exploration along the middle part of the CIR (MCIR; 8–17°S; Fig. 1a), which is a slow- to intermediate-spreading ridge (Pak et al. 2017). Eleven oceanic core complexes (OCC) have been recognised in the surveyed areas and generally exhibit hydrothermal plume signatures (Son

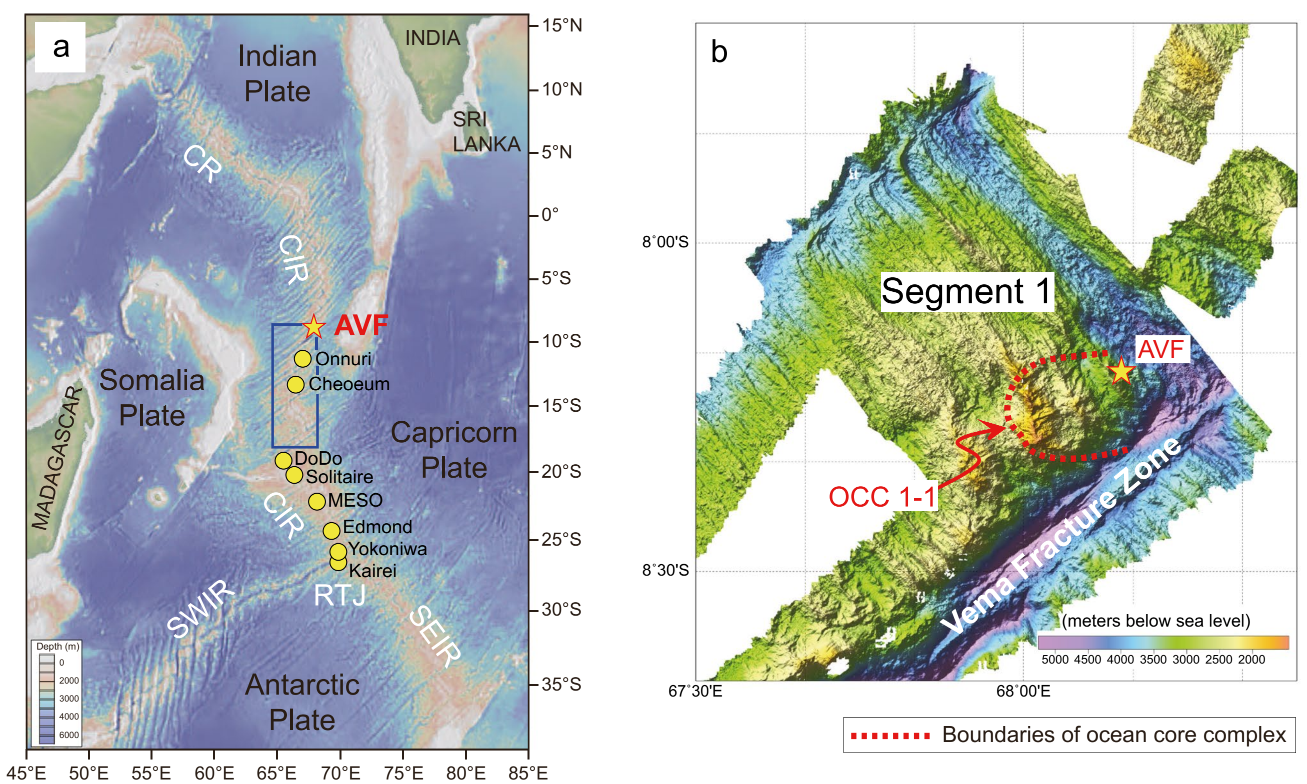

Fig. 1 **a** Tectonic boundaries and distribution of hydrothermal vent fields along the Central Indian Ridge (CIR). The blue box indicates the survey area. **b** Detailed bathymetric map of segment 1 of the middle part of the CIR. The location of the Ari vent field (AVF) at 8.15°S in oceanic core complex (OCC) 1-1 is marked by a yellow star. The dotted red line indicates the boundaries of the OCC 1-1. Abbreviations: CR, Carlsberg Ridge; MESO, MEteor-SOnne; RTJ, Rodriguez Triple Junction; SEIR, Southeast Indian Ridge; SWIR, Southwest Indian Ridge

et al. 2014; Pak et al. 2017). In OCC 1-1 (8.2°S), which shows methane concentrations of up to 13.01 nmol/L and nephelometric turbidity units of up to 0.16 (Pak et al. 2017; Kim et al. 2020), a new hydrothermal site, the Ari vent field (AVF), was discovered by a deep-towed camera during the hydrothermal expedition by R/V ISABU in 2018 (Fig. 1b).

In this study, we conducted a detailed mineralogical investigation and high-resolution geochemical analysis of AVF hydrothermal sulfide samples to characterise the distribution of trace elements and constrain the hydrothermal processes. We compared the geochemical data for pyrite and sphalerite from the AVF with those of other MOR-related SMS deposits and ancient volcanogenic massive sulfide (VMS) deposits in the Urals, in order to distinguish the differences in seafloor hydrothermal mineralisation between mafic- and ultramafic-hosted vent fields. The occurrences of serpentinised ultramafic rocks and reduced sulfide assemblages (pyrrhotite–isocubanite–chalcopyrite–Fe-rich sphalerite) and the distribution of Sn in pyrite and sphalerite indicate that the AVF is one of the few hydrothermal systems in the CIR to have an ultramafic affinity.

Ari vent field

The AVF (8°10.46´S, 68°08.29´E; water depth ~ 3700 m) is located on the OCC 1-1 at the southern inside corner of MCIR segment 1 (Fig. 1b). Its diameter is 150–200 m, as estimated by the deep-towed camera survey (Kim et al. 2020). Basement rocks collected from the OCC 1-1 consist of basalt, gabbro, microgabbro, and serpentinised harzburgite (Yi et al. 2014; Pak et al. 2017). This rock assemblage represents the exhumed lower oceanic crust and mantle, which likely had an important role in determining the redox state and metal contents of the AVF hydrothermal fluids.

The hydrothermal chimneys and mounds are mainly characterised by inactive venting, with diffuse venting being only observed intermittently (Fig. 2). Most chimneys are up to ~ 1.5 m high and, in many cases, are coalesced into a cluster (Fig. 2a). Sulfide mounds without chimney structures are common (Fig. 2b). A thick sediment layer typically covers the surfaces of the inactive chimneys and mounds, where evidence of life was generally absent during the camera survey (Fig. 2a–c). This is in contrast to the small amounts of sediment and abundant vent fauna that are typical of active vent fields in the CIR (Nakamura et al. 2012; Wang et al. 2014). Hydrothermal alteration zones are widespread in the AVF (Fig. 2d). The alteration zone is evident from a reddish brown and/or yellow colour and was likely caused by oxidation of metalliferous sediments by ambient seawater.

Samples

Hydrothermal sulfide, sulfide-bearing Fe-oxyhydroxide fragments, and consolidated metalliferous sediment samples were recovered using a TV-guided grab (GTV) from the AVF (Fig. 3). The hydrothermal sulfide samples can be classified into two different types according to the major sulfide minerals: (1) Fe–Cu-rich sulfides dominated by pyrite and isocubanite (samples GTV 180101 and 180,103; Fig. 3a, b) and (2) Cu-rich sulfides dominated by isocubanite (samples GTV 180102 and 180106; Fig. 3c, d). Samples

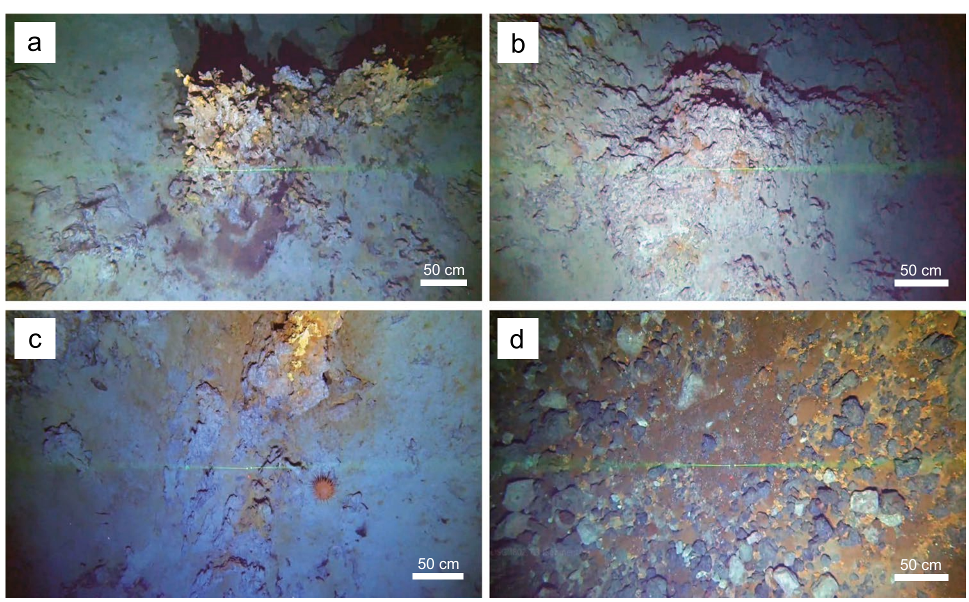

Fig. 2 Photographs of the Ari vent field. **a** Inactive chimneys coalesced into a cluster. **b** Hydrothermal mound covered by thick sediment layers. **c**, **d** Hydrothermal alteration zones with a reddish brown and/or yellow colour

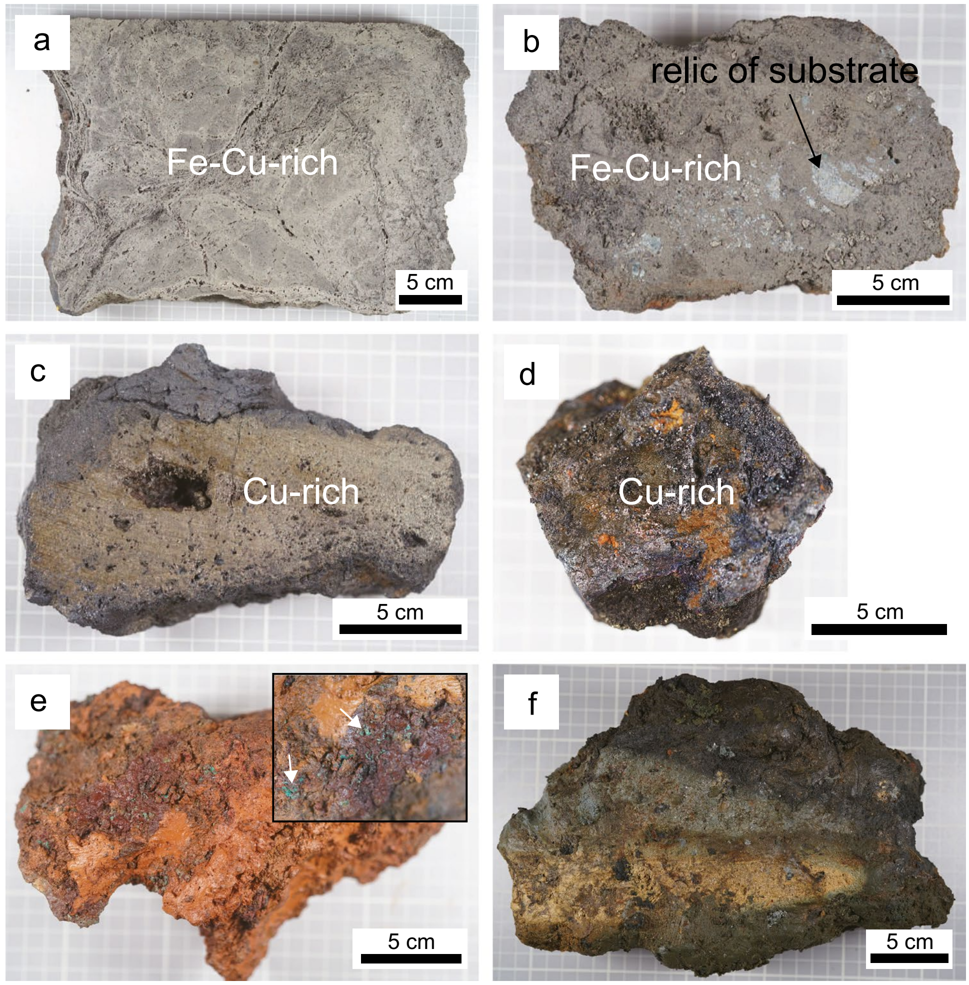

Fig. 3 Photographs of hydrothermal samples collected from the Ari vent field. Hydrothermal sulfides can be classified into two different types according to the major sulfide minerals: **a**, **b** Fe–Cu-rich sulfides and **c**, **d** Cu-rich sulfides, respectively. **e** Fe-oxyhydroxide fragment with secondary Cu minerals (white arrows). **f** Hydrothermally altered, consolidated sediment exhibiting variable degrees of alteration

GTV 180101 and 180103 have a massive texture, with some cavities being lined by pyrite (Fig. 3a, b). Some greenish fragments of basement rock are included in the matrix of sample GTV 180103 (Fig. 3b). Sample GTV 180102 shows distinct colour zonation (Fig. 3c). The exterior part in contact with seawater is thinly coated with a secondary chalcocite that is dark purple in colour. Sample GTV 180106 is one of the small fragments of Cu-rich sulfides and has a mineralogy similar to that of sample GTV 180102 (Fig. 3d; Table 1). Sample GTV 180202 consists mainly of Fe-oxyhydroxides with minor sulfides (Fig. 3e). X-ray diffraction (XRD) analysis shows peaks of atacamite, hematite, and goethite (ESM 1 Fig. S1). Sample GTV 180402 is consolidated metalliferous sediment that is common around other seafloor hydrothermal vents (Fig. 3f; Hannington et al. 2005). This sediment has various colours, reflecting variable degrees of hydrothermal alteration (Fig. 3f). The sulfide-bearing Fe-oxyhydroxide fragment (GTV 180202) and consolidated metalliferous sediment (GTV180402) samples are from a hydrothermal alteration zone (Fig. 2d).

Mineralogy and paragenesis

The sulfide samples are classified as Fe–Cu- and Cu-rich, based on the major sulfide minerals (Fig. 4; Table 1). We identified three stages of mineralisation based on the mineral assemblages and textures (Fig. 5).

Fe–Cu-rich sulfide samples

Magnetite (Mgt-A), pyrrhotite (Po-A), isocubanite (Icb-A), and chalcopyrite (Ccp-A) are early-formed minerals of stage I mineralisation (Figs. 4a–c and 5). Magnetite and pyrrhotite are commonly replaced by isocubanite (Fig. 4a, b). Chalcopyrite occurs mainly as exsolution lamellae within isocubanite and also as a few discrete grains (Fig. 4b). With progressive mineralisation, the pyrite increases in content and has two morphologically and mineralogically distinct generations (Fig. 4a–f). Subhedral to euhedral early pyrite (Py-A1) surrounds isocubanite and chalcopyrite, indicating that pyrite precipitated after Cu-sulfides (Fig. 4a, b). The early

Table 1 Mineral abundances of hydrothermal sulfides from the Ari vent field

Sample ID	GTV 180101	GTV 180103	GTV 180102	GTV 180106	GTV 180202
Type	Fe–Cu-rich sulfides		Cu-rich sulfides		Sulfide-bearing Fe-oxyhydroxide fragments
Pyrite/marcasite	+ + +	+ + +	+	tr	tr
Pyrrhotite	+	+	+	+	
Isocubanite	+ +	+	+ + +	+ + +	tr
Chalcopyrite	+	+	tr	+	tr
Sphalerite	+	tr	+	+ +	
Galena		tr			tr
Electrum		tr		tr	
Cobaltite			tr	tr	
Uraninite		tr			tr
Altered isocubanite phase			+	+	
Chalcocite	+	+	+ +	+ +	
Atacamite					+ + +
Magnetite		+			
Hematite					+ + +
Goethite					+ +

Volume percent determined by investigation of polished sections (tr = < 5%, + = 5–20%, + + = 20–50%, + + + = > 50%)

pyrite is often precipitated along fracture zones in chlorite grains, which are relics of basement rocks (Fig. 4c). Stage II mineralisation is represented by late colloform pyrite (Py-A2), sphalerite (Sp-A), and galena (Gn-A) (Fig. 4d, e). The late pyrite forms a lining structure associated with sphalerite (Fig. 4d). Galena fills some cavities in stage I sulfide minerals (Fig. 4e). Stage III is characterised by Fe–Cu-rich sulfide samples that have experienced seawater alteration. In particular, trace amounts of uraninite (< 1 µm in size; Urn-A) sporadically infill some cavities and/or are precipitated on altered surfaces of early pyrite during this mineralisation stage (Figs. 4f; ESM 1 S2a).

Cu-rich sulfide samples

Stage I mineralisation comprises mainly isocubanite (Icb-B) and sphalerite, along with minor pyrrhotite (Po-B), chalcopyrite (Ccp-B), and marcasite (Mrc-B) (Fig. 5; Table 1). Early-formed marcasite shows altered surfaces (Fig. 4g). Sphalerite is more abundant in the Cu-rich sulfide samples than in the Fe–Cu-rich sulfide samples (Table 1). In the former samples, sphalerite shows two different generations. Relics of early sphalerite (Sp-B1) containing numerous inclusions of isocubanite are rarely identified and are replaced by isocubanite (Fig. 4h). With progressive mineralisation, coarse-grained isocubanite becomes predominant, and chalcopyrite appears as exsolution lamellae within isocubanite (Fig. 4g–k). Late sphalerite (Sp-B2) commonly replaces isocubanite with chalcopyrite exsolution (Fig. 4i). Stage II mineralisation is characterised by trace amounts of cobaltite (Cbt-B) precipitated in cavities of isocubanite grains, which is sub- to euhedral (Fig. 4j; ESM 1 S2b). Electrum occurs as small inclusions (El-B; mostly < 1 µm) in cobaltite or infills the cavities in earlier-formed sulfides (Fig. 4j; ESM 1 S2b). Stage III mineralisation is characterised by chalcocite (Cct-B) and an altered isocubanite phase (Aip-B), which extensively replace earlier-formed isocubanite (Fig. 4g, k).

Sulfide-bearing Fe-oxyhydroxide fragment

The sulfide-bearing Fe-oxyhydroxide fragment consists mainly of atacamite (Atc-C), hematite (Hem-C), and goethite (Gth-C), along with trace pyrite (Py-C), isocubanite (Icb-C), chalcopyrite (Ccp-C), galena (Gn-C), and uraninite (Urn-C; Table 1; ESM 1 Fig. S1). Pyrite is replaced by hematite and/or goethite, whereas the other sulfides are present as submicroscopic inclusions in the Fe-oxyhydroxides (Fig. 4l). Uraninite is present as inclusions (< 1 µm in size) in hematite (Fig. 4l inset). All of these minerals are enclosed by later-formed atacamite (Fig. 4l).

Analytical methods

An optical microscope and XRD analysis were used for mineral identification and textural interpretation of the hydrothermal sulfide samples and sulfide-bearing

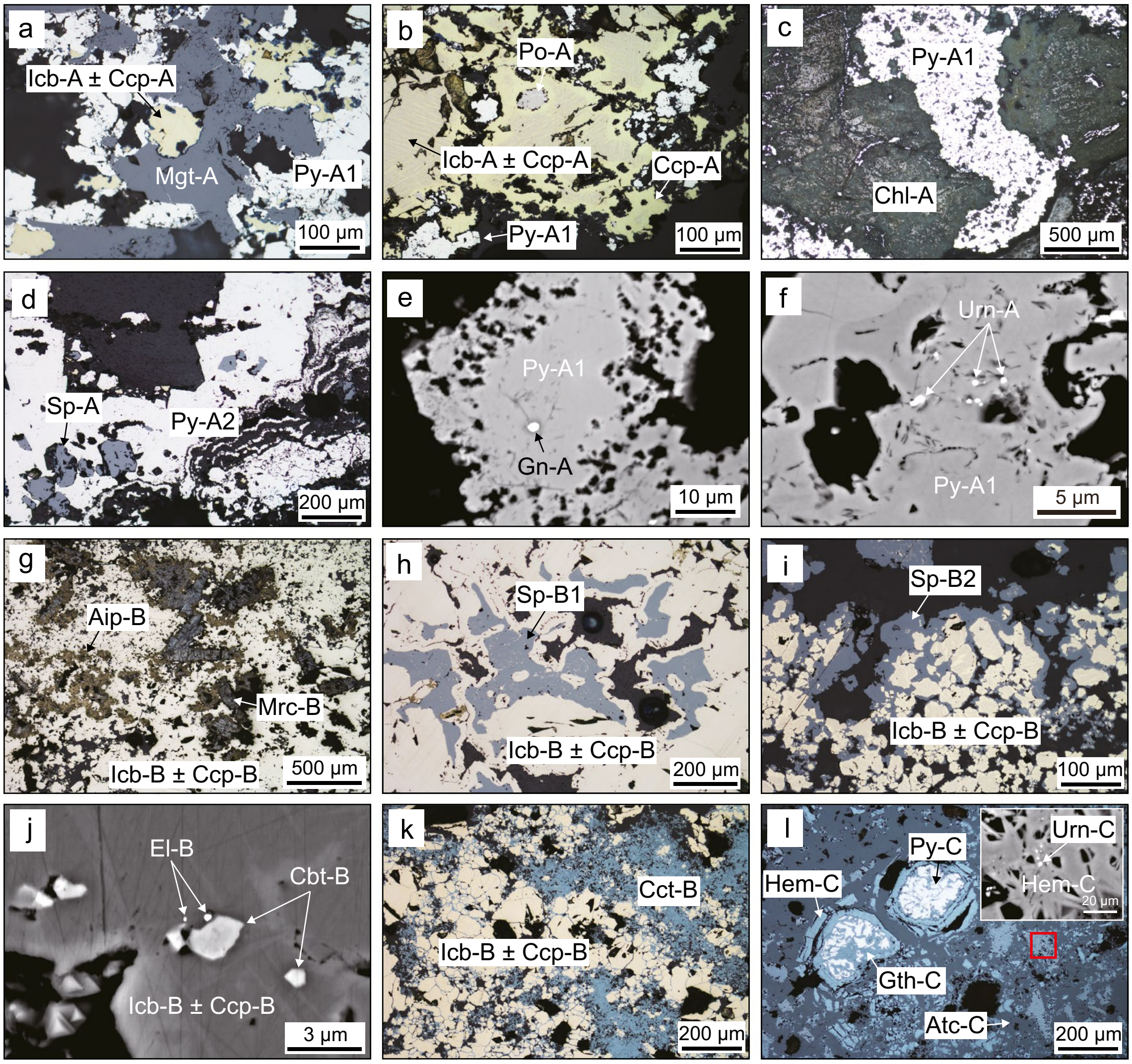

Fig. 4 Photomicrographs and backscattered-electron (BSE) images of sulfide mineral assemblages from the Ari vent field. **a**–**f** Fe–Cu-rich sulfide samples: **a** magnetite (Mgt-A) replaced by isocubanite (Icb-A); **b** subhedral–euhedral early pyrite (Py-A1) surrounding isocubanite and chalcopyrite (Ccp-A); **c** early pyrite precipitated along cracks and/or fractures in chlorite (Chl-A); **d** late colloform pyrite (Py-A2) associated with sphalerite (Sp-A); **e** galena (Gn-A) inclusion in an early pyrite grain; **f** uraninite (Urn-A) in early pyrite. **g**–**k** Cu-rich sulfide samples: **g** marcasite (Mrc-B) replaced by coarse-grained isocubanite–chalcopyrite (Icb-B–Ccp-B) aggregates; **h** relics of early sphalerite (Sp-B1) replaced by isocubanite–chalcopyrite aggregates; **i** late sphalerite (Sp-B2) replacing isocubanite–chalcopyrite aggregates; **j** cobaltite (Cbt-B) and electrum (El-B) in cavities of Cu sulfides; **k** chalcocite (Cct-B) extensively replacing earlier formed minerals. **l** Sulfide-bearing Fe-oxyhydroxide fragment with atacamite (Atc-C) surrounding pyrite (Py-C) replaced by goethite (Gth-C) and hematite (Hem-C). Abbreviations: Aip, altered isocubanite phase; Po, pyrrhotite; "A", "B", and "C" indicate minerals in the Fe–Cu-rich sulfides, Cu-rich sulfides, and sulfide-bearing Fe-oxyhydroxide fragment, respectively. The numbers indicate the generations of pyrite and sphalerite inferred from the textures and mineral assemblages

Fe-oxyhydroxide fragment, at KIOST, Busan, South Korea. The semiquantitative analyses of the mineralogy of 19 polished sections are presented in Table 1. XRD analysis was undertaken using a Panalytical X'Pert-PRO diffractometer with a CuKα X-ray source operated at 40 kV and 30 mA. The XRD patterns were recorded over a 2θ range from 5 to 65°, with a 0.01° step size and scan rate of 1°/min (ESM 1 Fig. S1).

Bulk chemical compositions of the hydrothermal sulfides were determined using Au–Ag Fire Assay, 4-Acid Digestion (Code 8 ICP–OES), and Peroxide Fusion Package (Ultratrace 7) at Actlabs (Ancaster, Ontario, Canada). The detection limits for each element are listed in Table 2.

Electron microprobe analysis (EPMA) of individual minerals was conducted using a JEOL JXA-8530F electron microprobe with an accelerating voltage of 15 kV, a beam

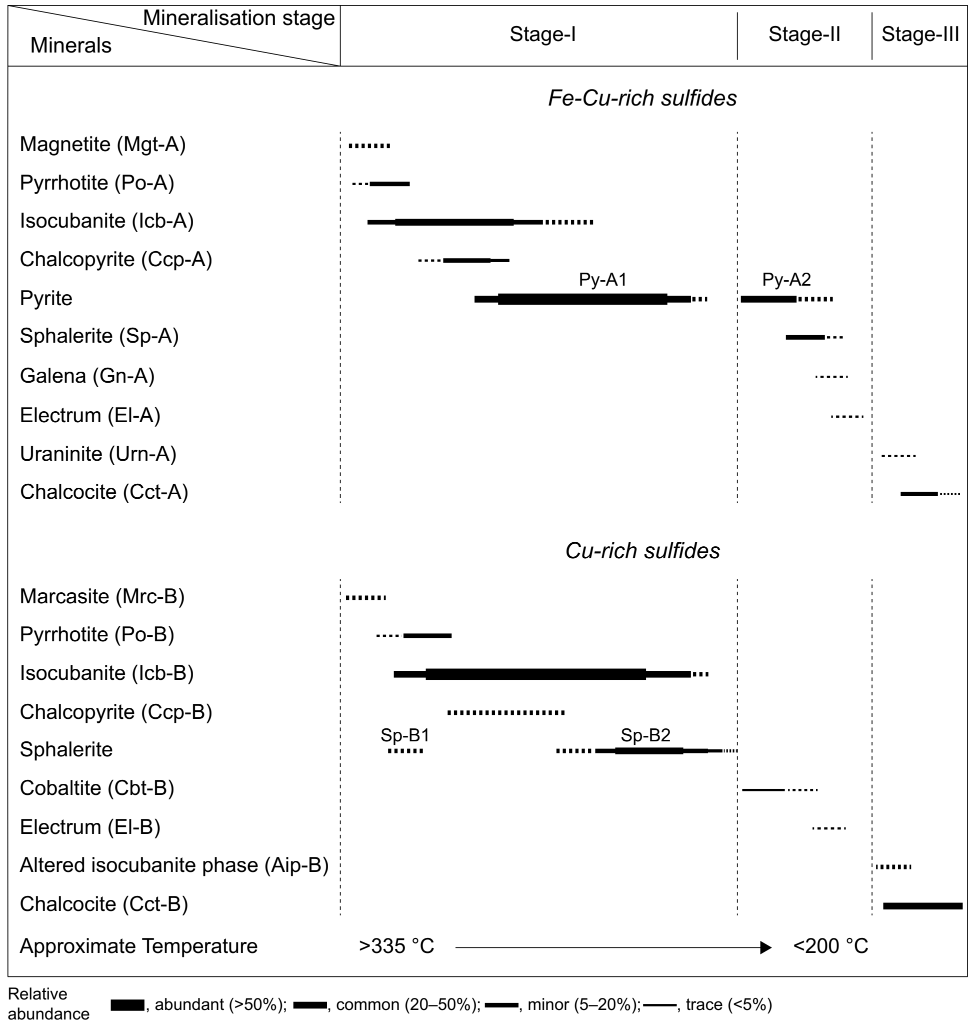

Fig. 5 Paragenesis of hydrothermal sulfides in the Ari vent field. Abbreviations are as in Fig. 4

current of 20 nA, and an electron beam diameter of 5 µm at Gyeongsang National University, Jinju, South Korea. Natural mineral and synthetic standards and Aztec software using ZAF corrections were used for the data calibration: FeS_2 (for Fe and S), ZnS (Zn), $CuFeS_2$ (Cu), PbS (Pb), CdS (Cd), Sb_2S_3 (Sb), InAs (In and As), and pure metal (Mn, Co, and Ni). Results of individual analyses are given in ESM 2 Table S1.

Laser ablation–inductively coupled plasma–mass spectrometry (LA–ICP–MS) analysis was undertaken with a 193-nm excimer LA system (ESI NWR 193, USA) coupled to an Agilent 7700 quadrupole ICP–MS instrument at KIOST. The laser beam diameter was 30–50 µm, depending on mineral grain size, the laser pulse rate was 10 Hz, and the laser energy was 5.7 J/cm^2. The total analysis time for each spot was 90 s, comprising 50 s of background measurement followed by 40 s of data acquisition during sample ablation. The following isotopes were measured: ^{55}Mn, ^{57}Fe, ^{59}Co, ^{60}Ni, ^{65}Cu, ^{66}Zn, ^{69} Ga, ^{74}Ge, ^{75}As, ^{77}Se, ^{95}Mo, ^{109}Ag, ^{111}Cd, ^{115}In, ^{118}Sn, ^{121}Sb, ^{125}Te, ^{197}Au, ^{205}Tl, ^{208}Pb, ^{209}Bi, and ^{238}U. Dwell times for each element were set to 0.02 s, except for Cu, Fe, and Zn, which were set to 0.01 s. External calibration was undertaken using STDGL3 (Belousov et al. 2014). The MASS-1 sulfide reference material (also known as PS-1; Wilson et al. 2002) was analysed as an unknown sample to assess the data quality (ESM 2 Table S2). The results yielded a relative standard deviation (RSD) of $<6\%$ for most elements. The Fe, Zn, and Cu contents determined by EPMA were used as internal standards for quantification of pyrite, sphalerite, and isocubanite, respectively. Contents of Ga and Hg were calculated using MASS-1 as a primary standard, because the Ga and Hg contents of STDGL3 are poorly constrained. The LA profiles for each element were monitored to identify the presence of micron-sized mineral inclusions. Spectra with spikes were not used to calculate trace-element contents. Data calculations were carried out using an in-house Excel spreadsheet and following the method described by Longerich et al. (1996). The entire dataset is presented in ESM 1 Fig. S3 and ESM 2 Tables S3–5.

Table 2 Bulk chemical compositions of hydrothermal sulfides from the Ari vent field. All data are individual analyses

Elements	Detection limit	Fe–Cu-rich sulfides				Cu-rich sulfides			
		GTV 180101-S1	GTV 180101-S2	GTV 180103-S1	GTV 180103-S2	GTV 180102-S1	GTV 180102-S2	GTV 180106-S1	GTV 180106-S2
weight percent									
Cu	0.001	1.58	2.39	3.10	1.70	33	20.5	25.5	20.3
Fe	0.003	43.9	44.1	42	43.1	33.8	42.5	34.2	38.2
Zn	0.001	0.09	0.89	0.02	0.01	0.48	0.52	0.23	5.67
part per million									
Pb	0.8	245	40.4	10	7.5	24.2	2.6	63.3	8.1
Au	0.03	1.09	< 0.03	< 0.03	0.1	< 0.03	< 0.03	3.22	< 0.03
Ag	3	33	28	< 3	< 3	28	29	18	80
As	5	137	90	8	12	124	37	105	5
Sb	2	9	12	< 2	< 2	5	< 2	5	< 2
Co	0.2	33.5	93.1	590	938	4230	3910	3950	3610
Ni	10	20	20	110	140	20	< 10	20	< 10
Se	0.8	2.7	6.1	68.3	147	265	298	215	374
Sn	0.5	10.2	6.4	5.7	2.1	56.3	28.5	86.4	24.2
In	0.2	0.3	0.2	1.2	3.2	33.9	46.3	33.1	49.9
Mo	1	174	225	80	155	18	5	12	13
Ba	3	183	25	7	4	14	4	3	< 3
Bi	2	< 2	< 2	5	8	18	10	15	12
Ga	0.2	1.3	0.7	2.6	2.7	17.2	9.7	27	8.6
Te	6	< 6	< 6	< 6	< 6	< 6	8	< 6	10
U	0.1	8.7	7.1	45.3	51.9	1.5	0.2	0.3	0.4

< below the detection limit

LA–ICP–MS elemental mapping was undertaken by ablating sets of parallel lines in a grid across each sample. Lines were ablated with a beam size of 9 µm. The spacing between the lines and scan speed was kept constant to match the laser spot size. A laser frequency of 10 Hz was used at a constant laser energy of 5.7 J/cm^2. The acquisition time for most elements was set to 0.02 s, but for major elements (Fe, Cu, and Zn), it was 0.01 s. Images were compiled and processed using Iolite software developed by WaveMetrics (Paton et al. 2011).

In situ sulfur isotope analyses of pyrite were conducted with a Neptune Plus multiple collector–ICP–MS (Thermo Fisher Scientific, Bremen, Germany) coupled to a 193-nm GeoLas HD excimer ArF LA system (Coherent, Göttingen, Germany) at the Wuhan Sample Solution Analytical Technology Company Limited, Hubei, China. Helium gas was used to transport the ablated materials into the plasma with a gas flow of 0.5 L/min. Ablation was performed with a laser beam diameter of 44 µm, laser pulse rate of 2 Hz for single spot analyses, and laser energy of 6 J/cm^2. To avoid matrix effects, a pyrite standard PPP-1 (Fu et al. 2016) was used as a reference material for correcting the pyrite data. In addition, the in-house reference materials pyrrhotite SP-Po-01 ($\delta^{34}S_{VCDT} = 1.4‰ \pm 0.4‰$) and pyrite SP-Py-01 ($\delta^{34}S_{VCDT} = 2.0‰ \pm 0.5‰$) were analysed repeatedly as unknowns to assess the data quality. The standard errors for PPP-1, SP-Po-01, and SP-Py-01 are ±0.08‰, ±0.08‰, and ±0.18‰ (2 SD), respectively.

Results

Bulk chemistry

The hydrothermal sulfide samples have Cu contents (1.6–33 wt%) that are much higher than those of Zn (0.01–5.67 wt%) and Pb (0.0008–0.025 wt%; Table 2). These data plot within the sediment-free MOR field, similar to those of other SMS deposits in the CIR (Fig. 6a). Cobalt, Ga, Se, In, and Sn are more concentrated in the Cu-rich sulfide samples as compared with the Fe–Cu-rich sulfide samples, whereas Ni, U, and Mo are more enriched in the latter (Fig. 6b–d; Table 2). The Co contents exhibit a strong positive correlation with Se contents ($R^2_{Co–Se} = 0.96$; Fig. 6b). The U contents are positively correlated with Mo contents ($R^2_{U–Mo} = 0.76$; Fig. 6c) but negatively correlated with Sn contents ($R^2_{U–Sn} = 0.75$; Fig. 6d).

A comparison with other MOR systems shows that high (Cu + Zn) and Sn contents are distinctive characteristics of ultramafic-hosted sulfides (Fig. 6e). The AVF hydrothermal sulfides are relatively poor in Sn compared to other ultramafic-hosted sulfides from the Mid Atlantic Ridge, but the Sn content is distinct between Cu-rich and Fe–Cu-rich sulfide samples (Fig. 6e, f). Copper-rich sulfide samples have an affinity with ultramafic-hosted systems, whereas Fe–Cu-rich sulfide samples are typical of MORB-hosted systems (Fig. 6e). Although Fe contents exhibit no systematic differences between these two types of hydrothermal systems, ultramafic-hosted sulfides, including the AVF sulfide samples, are characterised by a negative correlation between Fe and Sn contents ($R^2_{Fe–Sn} = 0.75$; Fig. 6f).

Chemical compositions of sulfide minerals

Pyrite

Trace element contents of pyrite were only obtained for the Fe–Cu-rich sulfide samples, because the highly altered marcasite in the Cu-rich sulfide samples produced irregular LA–ICP–MS spectra (Figs. 4g; ESM 1 S4a). Most pyrite in the Fe–Cu-rich sulfide samples has smooth LA–ICP–MS time-resolved elemental profiles, but some exhibit irregular spikes of U (ESM 1 Fig. S4b). Cobalt, Ni, Cu, Se, and Sn are more concentrated in early pyrite (Py-A1) as compared with late pyrite (Py-A2), whereas Mn and Tl are more enriched in the latter (ESM 1 Fig. S3). The Co contents generally increase with increasing Te, Se, and Ni, but decrease with increasing Mn and Tl (Fig. 7a–d; ESM 2 Table S3). Some data for Py-A1, which exhibit substantial depletion in Ni at a given Co content (Fig. 7c), also have relatively high Mn and Tl contents comparable to those of Py-A2 (Fig. 7d).

Sphalerite

The AVF samples are dominated by Fe-rich sphalerite, which shows no systematic variation in FeS contents between the Fe–Cu-rich sulfide samples (average = 29 ± 1.5 mol %) and Cu-rich sulfide samples (30 ± 3 mol %; ESM 2 Table S1). In contrast, the trace element contents of the AVF sphalerite are highly variable in the two different types of hydrothermal sulfide samples (ESM 1 Fig. S3), although LA–ICP–MS analysis of the early sphalerite (Sp-B1) in the Cu-rich sulfide samples could not be undertaken due to the large amounts of mineral inclusions (Fig. 4h). Late sphalerite (Sp-B2) in the Cu-rich sulfide samples contains more Co, Ge, As, Se, Ag, Hg, Pb, and Bi as compared with sphalerite (Sp-A) from the Fe–Cu-rich sulfide samples, whereas Mn and Sn are more enriched in the latter (ESM 1 Fig. S3 and ESM 2 Table S4).

The Se contents exhibit a strong positive correlation with Co ($R^2_{Se–Co} = 0.98$ for Sp-A and 0.63 for Sp-B2; Fig. 8a). The Sn contents differ between the Fe–Cu- and Cu-rich sulfide samples: (1) Sn has positive and negative correlations with Se contents in the Fe–Cu- and Cu-rich sulfide samples, respectively (Fig. 8b); (2) the Cu/Sn ratio is very close to ~ 2 in the Fe–Cu-rich sulfide samples, but the relationship is more variable at relatively low Sn contents in the Cu-rich sulfide samples (Fig. 8c); and (3) most individual

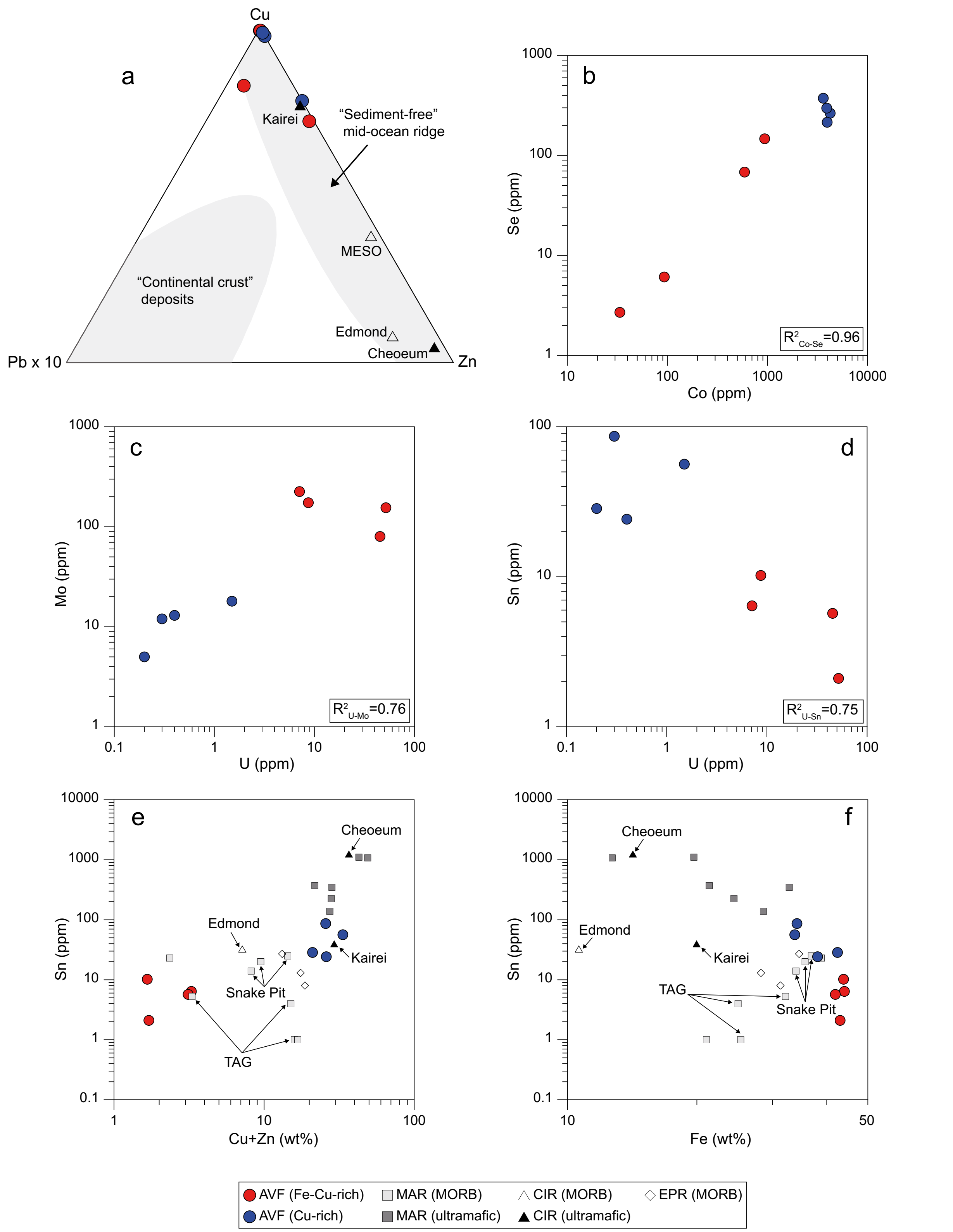

Fig. 6 Bulk chemical compositions of hydrothermal sulfides in the AVF. (**a**) Cu–Zn–Pb ternary diagram modified after Fouquet et al. (1993). Log–log plots of (**b**) Se versus Co, (**c**) Mo versus U, and (**d**) Sn versus U. (**e** and **f**) Detailed comparison of the Ari vent field with other SMS deposits from mid-ocean ridges: (**e**) Sn versus Cu + Zn and (**f**) Sn versus Fe. Average compositions of sulfides were taken from Hannington et al. (2005), Fouquet et al. (2010), Wang et al. (2014), Cao et al. (2018), Grant et al. (2018), Meng et al. (2020), and Choi et al. (2021). Abbreviations: EPR, East Pacific Rise; CIR, Central Indian Ridge; MAR, Mid-Atlantic Ridge; MESO, MEteor-SOnne; MORB, mid-ocean ridge basalt

Fig. 7 Trace element contents of pyrite determined by LA–ICP–MS. (**a**) Te versus Co, (**b**) Se versus Co, (**c**) Ni versus Co, and (**d**) Tl versus Mn. The dotted black lines indicate the below detection limit (bdl) of analysis. Abbreviations are as in Fig. 4

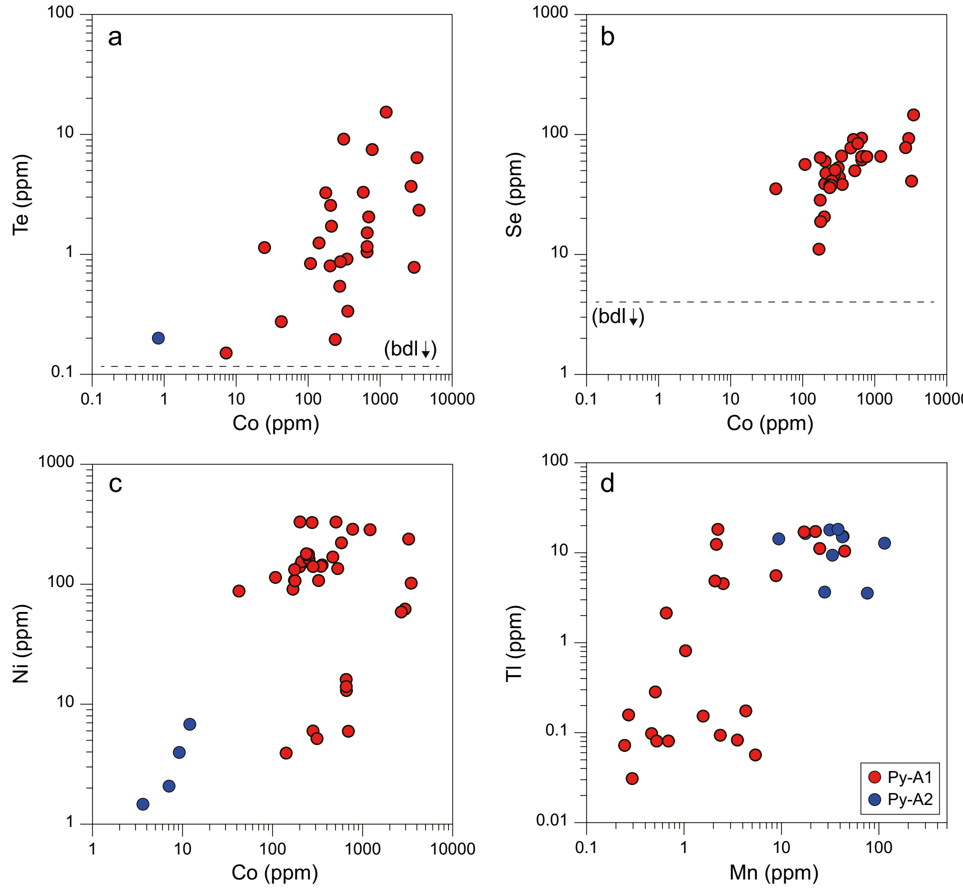

analyses of the Cu-rich sulfide samples lie on, or close to, the Ga:Sn = 1:1 line, but all data for the Fe–Cu-rich sulfide samples deviate from this line (Fig. 8d).

Isocubanite

The Co, Ga, Se, Ag, and In contents of isocubanite (Icb-B) in the Cu-rich sulfide samples are higher than those of isocubanite (Icb-A) in the Fe–Cu-rich sulfide samples, whereas Mn is more enriched in the latter (ESM 1 Fig. S3). The Se contents commonly increases with Co contents (Fig. 9a). In particular, Icb-B is characterised by systematic variations in Zn, Ga, Se, and Sn contents that differ from those of Icb-A (Fig. 9b–d). Specifically, Sn contents are negatively correlated with Se contents (Fig. 9b) but positively correlated with Ga and Zn contents for Icb-B (Fig. 9c, d).

LA–ICP–MS elemental mapping

Elemental maps were obtained for a Cu-rich sulfide sample to investigate the distribution of trace elements between adjacent minerals (ESM 1 Fig. S5). The maps show that Co, As, Ag, and Pb are incorporated preferentially into marcasite as compared with late sphalerite (Sp-B2) and isocubanite with chalcopyrite exsolution. In particular, the Ga and Sn contents appear to be zoned. The highest contents are confined to replacement boundaries between the late sphalerite and isocubanite with chalcopyrite exsolution.

Sulfur isotopic composition of pyrite

In situ S isotopic compositions ($n = 10$) of pyrite were obtained from Fe–Cu-rich sulfide samples in accordance with the different mineralisation stages (Fig. 5; Table 3). Early pyrite (Py-A1) has $\delta^{34}S = 6.2–8.5‰$ (average = 7.03‰), whereas late pyrite (Py-A2) has $\delta^{34}S = 6.6–6.7‰$ (average = 6.65‰; Table 3). The data overlap those of other MOR systems (Fig. 10).

Discussion

Mineralisation sequence and fluid evolution

The typical exterior–interior mineralogical zones and innermost vent conduits of seafloor chimneys are not observed in the hydrothermal sulfide samples (Fig. 3). In addition,

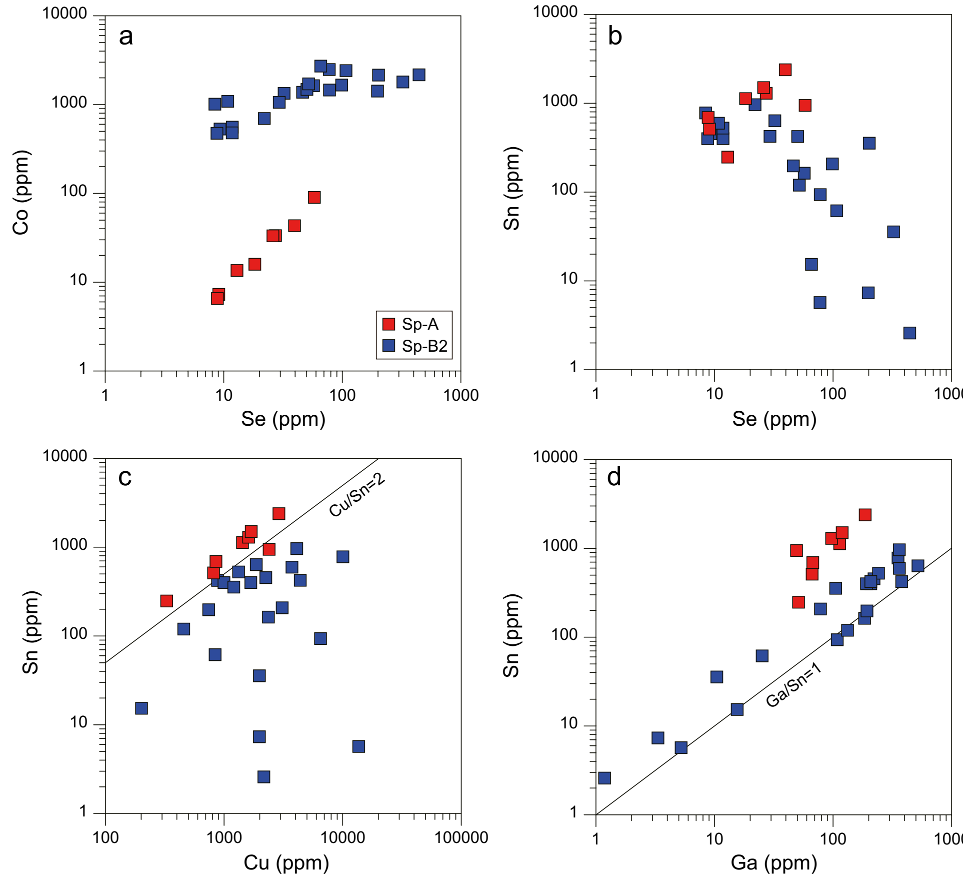

Fig. 8 Trace element contents of sphalerite determined by LA–ICP–MS. (**a**) Co versus Se, (**b**) Sn versus Se, (**c**) Sn versus Cu, and (**d**) Sn versus Ga. The solid black lines indicate data correlation trends. Abbreviations are as in Fig. 4

the matrix of sample GTV 180103 contains some greenish fragments of basement rock (Fig. 3b). These results indicate that the collected samples correspond to massive sulfide mounds taken from slightly different locations. Petrographic investigations reveal that Fe–Cu-rich sulfide samples underwent three different stages of mineralisation with decreasing fluid temperature and fS_2 and increasing fO_2 (Figs. 4 and 5): subhedral–euhedral pyrite (Py-A1) and isocubanite (Icb-A) dominates stage I; colloform pyrite (Py-A2) and sphalerite (Sp-A) dominates stage II; and stage III represents seawater alteration. The Cu-rich sulfide samples have mineral assemblages and a paragenesis similar to those of the Fe–Cu-rich sulfide samples, but the much higher amount of isocubanite indicates relatively reducing and high-temperature conditions during deposition of the former (Fig. 5; Table 1; Kawasumi and Chiba 2017). This is consistent with LA–ICP–MS analysis showing that the Co and Se contents of sphalerite and isocubanite are higher in the Cu-rich sulfides than in the Fe–Cu-rich sulfides (Figs. 8a and 9a; ESM 2 Tables S4 and 5), given that enrichments in these elements are typical of relatively high-temperature sulfide minerals because the solubility of Co and Se in vent fluids decreases abruptly at temperatures of < 350 °C (Huston et al. 1995; Butler and Nesbitt 1999; Metz and Trefry 2000; Maslennikov et al. 2009; Keith et al. 2016; Meng et al. 2020).

LA–ICP–MS analyses show that the trace element contents of pyrite vary in the different mineralisation stages (Fig. 7; ESM 1 S3). Cobalt, Se, and Ni are enriched in early pyrite (Py-A1) as compared with late pyrite (Py-A2), whereas Mn and Tl are more enriched in the latter (Fig. 7; ESM 2 Table S3). Previous studies have suggested that high contents of Mn and Tl are good indicators of low-temperature mineralisation (< 200 °C; Maslennikov et al. 2009; Meng et al. 2020). As such, the Co–Se-rich early pyrite from the AVF was precipitated from relatively high-temperature fluids as compared with Mn–Tl-rich late pyrite (Fig. 7). However, the temperature dependency cannot explain the enrichment of Ni in early pyrite relative to late pyrite (ESM 2 Table S3), as Ni is typically incorporated into the crystal lattice of pyrite during relatively low-temperature mineralisation (Maslennikov et al. 2009; Keith et al. 2016). The Ni contents of the early pyrite are highly variable at a given Co content (Fig. 7c), suggesting that the fluid temperature was not a major control on the Ni contents of the AVF pyrite. Alternatively, a high fS_2 of hydrothermal fluids is known to enhance the incorporation of Ni into pyrite (Maslennikov et al. 2009; Li et al. 2017). We suggest that the main-stage mineralisation corresponding to stage I was associated with high fS_2, thereby enhancing the substitution of Ni into early pyrite (Figs. 5 and 7c). As mineralisation proceeded, the

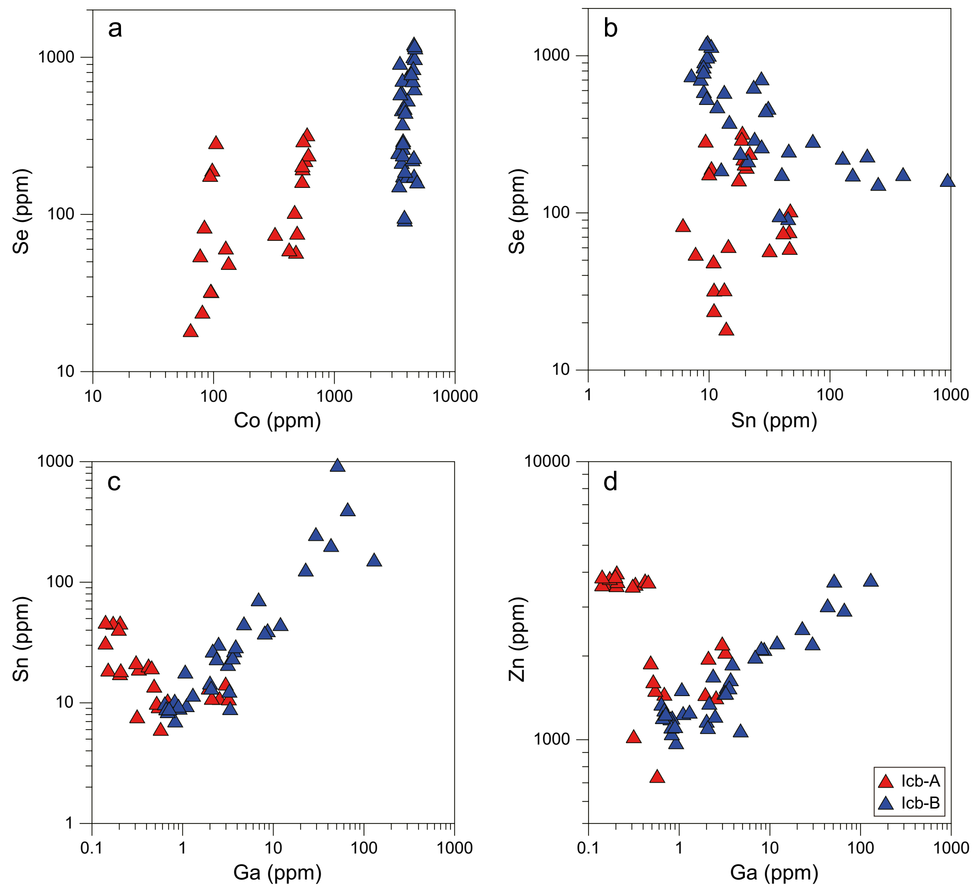

Fig. 9 Trace element contents of isocubanite determined by LA–ICP–MS. (**a**) Se versus Co, (**b**) Se versus Sn, (**c**) Sn versus Ga, and (**d**) Zn versus Ga. Abbreviations are as in Fig. 4

Table 3 In situ S isotopic compositions of pyrite in the Fe–Cu-rich sulfide samples

Spot no	Mineral	$\delta^{34}S_{V\text{-}CDT}$ (‰)	Error (2σ)	Proportions of sulfur sources (%)	
				Seawater-derived	Igneous origin
G1801-1	Early pyrite (Py-A1)	8.5	0.1	40.4	59.6
G1801-2		7.7	0.09	36.5	63.5
G1801-3		6.5	0.12	30.8	69.2
G1801-4		6.8	0.08	32.2	67.8
G1801-5		6.4	0.15	30.3	69.7
G1803-1		6.2	0.16	29.3	70.7
G1803-2		7.5	0.11	35.6	64.4
G1803-3		6.6	0.13	31.3	68.8
G1801-6	Late pyrite (Py-A2)	6.7	0.1	31.7	68.3
G1801-7		6.6	0.1	31.3	68.8

V-CDT Vienna-Canyon Diablo Troilite

influx of ambient seawater may have decreased the fS_2 and temperature of the hydrothermal fluids, which ultimately led to the relatively Ni-poor compositions of some early pyrite (Fig. 7c). This is supported by the Ni-poor early pyrite that has relatively high Mn and Tl contents similar to those of late pyrite (Fig. 7d). These results indicate that the Ni contents of the AVF pyrite were likely controlled by fS_2 rather than the fluid temperature.

Seafloor hydrothermal deposits with an ultramafic affinity are typically characterised by CH_4- and H_2-rich and H_2S-poor hydrothermal fluids as compared with MORB-hosted SMS deposits (Charlou et al. 2002;

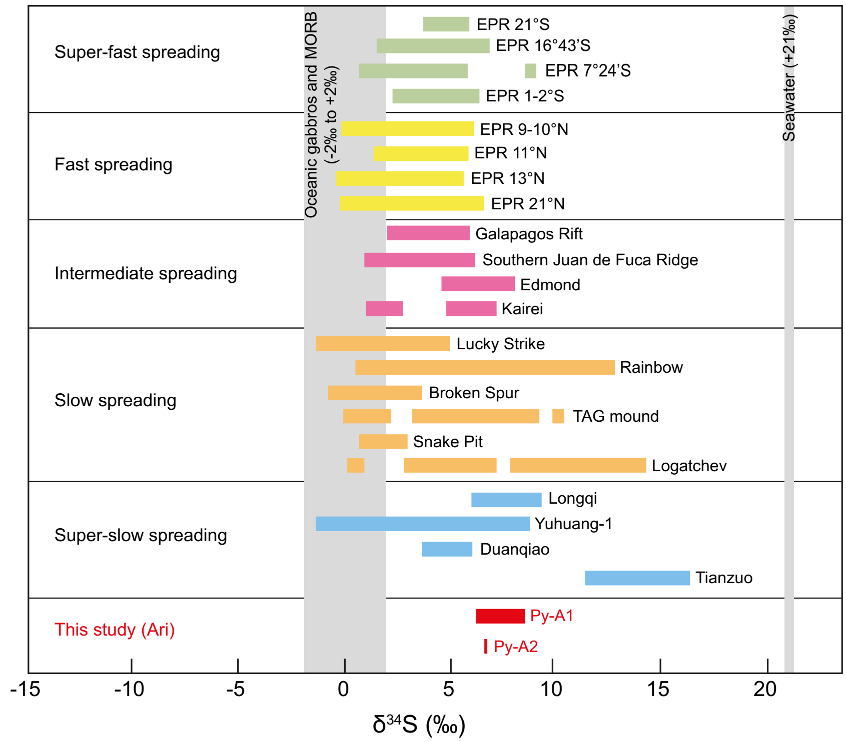

Fig. 10 Sulfur isotope composition of different generations of pyrite in the Ari vent field. Ranges of $\delta^{34}S$ values of other MOR systems are modified from Zeng et al. (2017). Other data are from the following: Ding et al. (2021); Tianzuo (Cao et al. 2021); Yuhuang-1 (Liao et al. 2018); seawater (Rees et al. 1978); MORBs (Sakai et al. 1984); gabbro (Alt et al. 1989, 2007; Alt and Anderson 1991

Nakamura et al. 2009; Schmidt et al. 2011), indicative of low fO_2–fS_2 environments. Such a low redox potential and fS_2 of the AVF hydrothermal fluids is consistent with other lines of geochemical and mineralogical evidence. The AVF sphalerite has high FeS contents (26.6–36.5 mol %), irrespective of the two types of hydrothermal sulfide samples (ESM 2 Table S1). These values are higher than those of many MORB-hosted systems (mostly < 25 mol % FeS; Graham et al. 1988; Hannington et al. 1991; Kawasumi and Chiba 2017), indicating that low fO_2–fS_2 conditions facilitated the incorporation of Fe into the crystal lattice of the AVF sphalerite (Scott and Barnes 1971; Kawasumi and Chiba 2017). The AVF sulfide samples have a mineral assemblage of pyrrhotite–isocubanite–chalcopyrite–Fe-rich sphalerite, which is common for other ultramafic-hosted SMS deposits in MOR settings (Fig. 5; Fouquet et al. 2010; Melekestseva et al. 2014; Wang et al. 2014; Choi et al. 2021). A previous experimental study showed that isocubanite began to form, intergrown with chalcopyrite and pyrrhotite, at 335 °C (Lusk and Bray 2002). This is consistent with isocubanite thermometry, which yielded an average formation temperature of ~ 365 °C for the ultramafic-hosted Cheoeum vent field, CIR (Choi et al. 2021). As such, the mineral assemblage in the AVF is indicative of highly reducing conditions and a formation temperature of > 335 °C. In addition, the magnetite replaced by isocubanite appears to be a high-temperature mineral of primary origin during mineralisation stage I (Fig. 4a). A previous study suggested that very low fO_2–fS_2 fluid conditions and low H_2S contents allow magnetite to precipitate in Cu–Fe-rich submarine hydrothermal chimneys (Fouquet et al. 2010).

The redox state of the AVF hydrothermal fluids varied significantly between different samples and mineralisation stages. For example, enrichments of Co and Se in sphalerite and isocubanite from the Cu-rich sulfide relative to the Fe–Cu-rich sulfide samples indicate that the former samples were formed under more reducing, high-temperature mineralisation, given that these elements are typical of sulfide minerals precipitated from such conditions (ESM 2 Tables S4 and 5; Huston et al. 1995; Butler and Nesbitt 1999; Maslennikov et al. 2009; Keith et al. 2016; Meng et al. 2020; Choi et al. 2023). In particular, substantial enrichment of Te in early pyrite (0.15 – 15.3 ppm) relative to late pyrite (mostly below detection limits) suggests that relatively reducing fluids produced the early pyrite (Figs. 7a; ESM 1 S3), given that a significant decrease in Te solubility can be caused by low fO_2 conditions (Grundler et al. 2013).

Our results indicate that the AVF sulfide samples were mainly formed by reducing, high-temperature fluids associated with an ultramafic-hosted hydrothermal system. This is consistent with the fact that serpentinisation of ultramafic rocks produces H_2- and CH_4-rich fluids, resulting in highly reducing conditions (Charlou et al. 2002; Nakamura et al. 2009; Schmidt et al. 2011). The sulfide samples are characterised by three different temporal variations in sulfide minerals with decreasing fluid temperature and fS_2 and increasing fO_2 from the main mineralisation stage I (> 335 °C) to relatively low-temperature mineralisation stage II (< 200 °C) and seawater alteration stage III (Fig. 5). This variable mineralisation is readily achieved by mixing between the reducing, high-temperature fluids, and ambient oxidised seawater as mineralisation progressed. However, compared with other ultramafic-hosted sulfides, the AVF sulfide samples have significant differences in U and Sn contents as described below (Fig. 6c–f; Table 2; Fouquet et al. 2010).

Uranium mineralisation

The Fe–Cu-rich sulfide samples and sulfide-bearing Fe-oxyhydroxide fragment contain discrete uraninite inclusions (Fig. 4f, l; ESM 1 S2a). In particular, the Fe–Cu-rich sulfide samples are enriched in Mo (80–225 ppm) and U (7.1–51.9 ppm) as compared with the Cu-rich sulfide samples (Fig. 6c; Table 2). These characteristics suggest that ambient seawater could be a principal source of elevated U content in the AVF, given that submarine hydrothermal fluids are substantially depleted in Mo (mostly < 10 nM) relative to seawater (average = 104 nM; Douville et al. 2002). We suggest that the weak hydrothermal activity (i.e., the predominance of inactive venting; Fig. 2) in the AVF had an important role in the formation of gossan-like altered zones on the seafloor (Maslennikov et al. 2012; Ayupova et al. 2018), which may have increased the U contribution of seawater. It is also considered that seawater circulating through the oceanic crust extracts U. As such, the pristine fluids expelled at the seafloor are U-poor, thereby forming sulfide minerals that are depleted in U (Hegner and Tatsumoto 1989; Mills et al. 1994; Butler and Nesbitt 1999). This is consistent with our LA–ICP–MS analyses, which showed that the AVF sulfide minerals are mostly depleted in U (< 0.5 ppm; ESM 2 Tables S3–5). Although some analyses of early pyrite (Py-A1) in the Fe–Cu-rich sulfide samples are characterised by anomalously high U contents of up to 12.2 ppm (ESM 2 Table S3), the irregular spikes of U in the LA–ICP–MS depth profiles reflect the presence of U-bearing inclusions within Py-A1 (ESM 1 Fig. S4b). Therefore, we suggest that the U contents of the AVF were mainly controlled by the precipitation of uraninite. The uraninite is mainly deposited on the altered surfaces of pyrite and/or hematite (Fig. 4f, l; ESM 1 S2a). Given the thick sediment layers, widespread hydrothermal alteration zones, and abundance of atacamite, chalcocite, hematite, and goethite around the inactive chimneys and/or mounds, protracted submarine weathering occurred in the AVF (Fig. 2; Table 1). As such, the oxidative alteration of Fe-bearing minerals may have facilitated the reduction of U from the hexavalent to tetravalent state, thereby enabling precipitation of uraninite inclusions (Fig. 4f, l; ESM 1 S2a). This is consistent with previous studies that suggested the fixation of seawater-derived U can be induced by the oxidation of Fe minerals (Mills et al. 1994; Ayupova et al. 2018).

Tin mineralisation

In the AVF sulfide samples, sphalerite (average 519 ± 524 ppm Sn; up to 2386 ppm Sn) and, to some extent, isocubanite (average 54.3 ± 135 ppm Sn; up to 939 ppm Sn) are substantially enriched in Sn as compared with pyrite (up to 16.2 ppm Sn; ESM 1 Fig. S3 and ESM 2 Tables S3–5), indicating that sphalerite and isocubanite are the main carriers of Sn in the AVF. This is consistent with the fact that Sn-rich, ultramafic-hosted SMS deposits are characterised by high Cu and Zn contents as compared with Sn-poor MORB-hosted sulfide deposits (Fig. 6e).

The Sn contents of the AVF sphalerite exhibit positive and negative correlations with Se in the Fe–Cu-rich (Sp-A) and Cu-rich sulfide samples (Sp-B2), respectively (Fig. 8b). As such, the sphalerite Sn contents cannot be explained by fluid temperature, as Se enrichments are typical of high-temperature sulfide minerals (Huston et al. 1995; Butler and Nesbitt 1999; Maslennikov et al. 2009; Meng et al. 2020; Choi et al. 2023). With some exceptions, Sn, Cu, and Ga contents are positively correlated with each other in the AVF sphalerite (Fig. 8c, d). In particular, the values of Cu/Sn = 2 and Ga/Sn = 1 reflect the control of sphalerite Sn contents being due to the coupled substitutions $3Zn^{2+} \leftrightarrow 2Cu^{+} + Sn^{4+}$ and $3Zn^{2+} \leftrightarrow Cu^{+} + Sn^{2+} + Ga^{3+}$, respectively (Cook et al. 2009; Ye et al. 2011). This suggests that determining the oxidation state of Sn (i.e., divalent versus tetravalent) is important for constraining the possible controls on sphalerite Sn contents due to lattice substitution. However, the Sn contents of the AVF sphalerite differ between the Fe–Cu- and Cu-rich sulfide samples. For the former, most data for Sp-A have Cu/Sn ~ 2, whereas most data for Sp-B2 from the Cu-rich sulfide samples have Cu/Sn < 2, especially at relatively low Sn contents (Fig. 8c). This suggests that the incorporation of Sn^{4+} into sphalerite may be facilitated by relatively oxidising, low-temperature conditions, given that Sp-A is found together with colloform pyrite in the late mineralisation stage II (Figs. 4d and 5), whereas Sp-B2 is precipitated with coarse-grained isocubanite in the main mineralisation stage I (Figs. 4h and 5). In contrast, the positive correlation between Ga and Sn contents with Ga/Sn = 1 is limited to Sp-B2 (Fig. 8d). This suggests that the preferential substitution of $3Zn^{2+} \leftrightarrow Cu^{+} + Sn^{2+} + Ga^{3+}$ occurs under relatively reducing, high-temperature conditions. These results suggest that the redox state of hydrothermal fluids is an important control on the Sn contents of sphalerite. Considering the much higher Sn contents of Sp-A relative to Sp-B2 (ESM 2 Table S4), Sn^{4+} is likely the most important form involved in the generation of Sn-rich sphalerite.

Systematic variations in Sn contents are only observed in isocubanite (Icb-B) in the Cu-rich sulfide samples and not in the isocubanite (Icb-A) in the Fe–Cu-rich sulfide samples (Fig. 9b–d). The Sn contents are negatively correlated with Se contents in Icb-B (Fig. 9b), although these elements are typical of relatively high-temperature Cu sulfide minerals (Hutchison and Scott 1981; Huston et al. 1995; Maslennikov et al. 2009). This indicates that fluid temperature had little effect on Sn contents in the AVF isocubanite. In contrast, Sn, Ga, and Zn contents in Icb-B are positively correlated with each other (Fig. 9c, d). The LA–ICP–MS depth profiles are typically flat, suggesting that these elements are present in Icb-B in solid solution. In particular, relics of early sphalerite (Sp-B1) occur within Icb-B (Fig. 4h). This indicates that the early formed Sp-B1 may have been dissolved and re-precipitated by the continuously ascending hydrothermal fluids. The LA–ICP–MS elemental maps also show that Ga and Sn are concentrated in bands along replacement boundaries between Sp-B2 and Icb-B in the Cu-rich sulfide sample (ESM 1 Figs. S5 and 6). Choi et al. (2021) suggested that these Sn–Ga-rich bands formed because these elements were no longer incorporated into the Cu minerals via coupled dissolution and re-precipitation. Although it cannot be completely excluded that the fluids that precipitated Icb-B were initially enriched in Sn and Ga, earlier formed sphalerite may have been one of the sources of Sn for the subsequent remobilisation process, given that the Sn and Ga contents of Icb-B are positively correlated with Zn (Fig. 9c, d). Our results suggest that the redox state of hydrothermal fluids and/or coupled dissolution and reprecipitation of previously deposited Sn-bearing sulfides could be more important factors controlling the Sn content compared to the fluid temperature.

Although the AVF sphalerite and isocubanite are enriched in Sn (ESM 1 Fig. S3), bulk chemical compositions show that the Sn contents differ for the two different types of AVF sulfide samples (Fig. 6d–f). High Sn contents, comparable to those of other ultramafic-hosted sulfides, are confined to the Cu-rich sulfide samples, whereas the Fe–Cu-rich sulfide samples are characterised by an affinity with MORB-hosted sulfides due to the significant Sn depletion (Fig. 6e). This indicates that further explanation is required to account for the anomalous Sn distribution in the Fe–Cu-rich sulfide samples. We suggest that ultramafic-hosted SMS deposits are likely to be depleted in Sn if they are dominated by Fe-rich mineralisation, given that the Fe–Cu-rich sulfide samples in the AVF consist mainly of Sn-poor pyrite (mostly < 1 ppm) (Table 1; ESM 1 Fig. S3). This is consistent with the bulk chemical compositions of other ultramafic-hosted SMS deposits at MOR settings, which exhibit a negative correlation between Sn and Fe contents (Fig. 6f).

Distribution of Sn in pyrite and sphalerite: a comparison of hydrothermal sulfides at MOR settings

In MOR-related hydrothermal systems, one of the most pronounced differences is the much higher Sn contents of ultramafic-hosted SMS deposits relative to MORB-hosted sulfide deposits (Fouquet et al. 2010; Wang et al. 2014; Evrard et al. 2015; Choi et al. 2021). However, it is still unclear why Sn enrichment is associated primarily with ultramafic-hosted hydrothermal mineralisation and which mineral(s) is the main Sn host.

To better understand the distribution of Sn on the mineral scale, we undertook a comparison of pyrite and sphalerite from different types of hydrothermal vent fields (i.e., MORB- versus ultramafic-hosted) in MOR settings (Fig. 11), given that pyrite and sphalerite are major constituents of SMS deposits and can incorporate various trace elements (Maslennikov et al. 2009; Keith et al. 2016; Meng et al. 2020). Sphalerite is substantially enriched in Sn (average > 1000 ppm), whereas most pyrite has very low average Sn contents (< 1 ppm) (Fig. 11). This indicates that sphalerite is one of the main Sn hosts, whereas pyrite is Sn-poor in ultramafic-hosted SMS deposits. Most of the ultramafic-hosted pyrite and sphalerite are enriched in Sn as compared with those in MORB-hosted deposits (Fig. 11). This difference suggests that hydrothermal fluids circulating through ultramafic lithologies could be a more efficient source of Sn as compared with MORB-related hydrothermal fluids. We suggest that the low redox potential of hydrothermal fluids in ultramafic-hosted systems could be important in enhancing the transport of $SnCl_2$ (Sn^{2+}) during hydrothermal circulation. As such, hydrothermal fluids are likely to precipitate Sn-rich minerals in ultramafic-hosted systems. This is consistent with the study of Schmidt et al. (2011) that reported the Sn concentrations of hydrothermal fluids are two orders of magnitude higher in the ultramafic-hosted Nibelungen vent field as compared with the MORB-hosted Red Lion vent field. Therefore, the Sn contents of the AVF pyrite and sphalerite, which are within the range of other ultramafic-hosted systems (Fig. 11), indicate that an ultramafic-hosted hydrothermal system had an important role in forming the AVF.

Our comparison also shows that Se contents of pyrite and sphalerite differ in the different types of hydrothermal chimneys (i.e., Cu- versus Zn-rich) in the same vent field, although they are not distinguishable between MORB- and ultramafic-hosted vent fields (Fig. 11). For example, pyrite and sphalerite from the Snake Pit and Rainbow sites have elevated Se contents in Cu-rich rather than Zn-rich chimneys (Fig. 11). Huston et al. (1995) demonstrated that mixing of

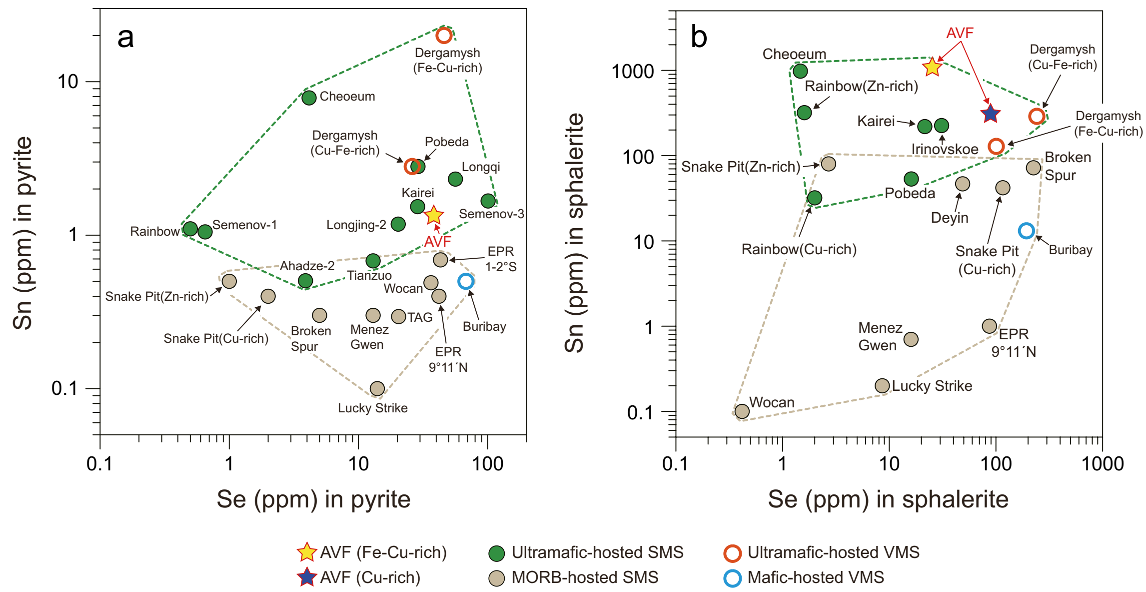

Fig. 11 Average contents of Sn and Se in (**a**) pyrite and (**b**) sphalerite for MORB- and ultramafic-hosted vent fields at MOR settings and mafic- and ultramafic-hosted VMS deposits in the Urals. All data were determined by LA–ICP–MS. Average compositions of sulfide minerals are from Maslennikov et al. (2017, 2020), Wang et al. (2017, 2018), Grant et al. (2018), Melekestseva et al. (2018, 2020a, b), Yuan et al. (2018), Meng et al. (2020), Choi et al. (2021), Liao et al. (2021), Ren et al. (2021) and Ding et al. (2022). Contents in parentheses indicate the different types of chimneys in the same vent field

fluids with seawater substantially lowers the Se contents of pyrite. In addition, high Se contents of sulfide minerals are commonly related to relatively reducing, high-temperature mineralisation (Butler and Nesbitt 1999; Maslennikov et al. 2009; Meng et al. 2020). Therefore, the relatively low Se contents of pyrite and sphalerite formed by Zn-rich mineralisation are likely due to the extent of seawater mixing, given that seawater can decrease the temperature and increase the redox potential of hydrothermal fluids. In contrast to Se, Sn-rich sulfide minerals are limited to Zn-rich chimneys in the same vent field (Fig. 11). This suggests that Sn-rich sulfide minerals form from relatively oxidising, low-temperature fluids. Our results show that sphalerite is one of the major host minerals of Sn (Figs. 11b; ESM 1 S3) and, in sphalerite, a much higher proportion of Sn may be precipitated in its tetravalent rather than divalent state (Fig. 8c, d; Cook et al. 2009; Ye et al. 2011; Choi et al. 2021). Given that Sn exists mainly as an Sn(II) aqueous complex (i.e., $SnCl_2$) in hydrothermal fluids (Uchida et al. 2002; Migdisov and Williams-Jones 2005), the oxidative transition from Sn(II) to Sn(IV) for Sn precipitation in sphalerite may have been facilitated by the relatively oxidising, low-temperature conditions. This is also consistent with the higher Sn contents of sphalerite in the Fe–Cu-rich sulfide samples as compared with the Cu-rich sulfide samples (Fig. 11b; ESM 1 S3).

It is generally considered that Fe^{2+} substitutes for Zn^{2+} within the sphalerite lattice (Keith et al. 2014; George et al. 2016). Concentrations of Fe and Sn in the AVF sphalerite exhibit a better positive correlation in the Cu-rich sulfide samples ($R^2 = 0.45$) as compared with the Fe–Cu-rich sulfide samples (ESM 1 Fig. S7). This suggests that the direct substitution of Sn^{2+} for Zn^{2+} may have been facilitated in the former by the relatively reducing conditions. These features further suggest that the oxidation state of Sn is likely an important control on Sn contents in sphalerite. Our results and comparison allow us to conclude that the geochemistry of pyrite and sphalerite, particularly for Sn, is a more effective approach than bulk compositional analysis of hydrothermal samples for tracing the nature and origins of ultramafic-hosted mineralisation in MOR settings, as the mineralogical compositions of hydrothermal sulfide samples are highly variable in each vent field.

Comparison with VMS deposits on land: genetic and economic implications

It has been widely accepted that seabed hydrothermal venting and its mineralisation are the modern analogues of VMS deposits on land (Maslennikov et al. 2017; Martin et al. 2021). The VMS deposits represent a significant source of the world's Cu, Zn, Pb, Au, and Au ores, with Co and Sn as by-products (Barrie and Hannington 1999; Hannington et al. 2010). They are conventionally classified into five groups based on host rock compositions: mafic, mafic-siliciclastic, bimodal-mafic, bimodal-felsic, and bimodal-siliciclastic types (Barrie and Hannington 1999).

The extensive seafloor exploration during the last two decades recognized the ultramafic-hosted SMS (UM-SMS) deposits (Fouquet et al. 2010; Choi et al. 2021). This contributed to the reclassification of some VMS deposits on land into a sub-class of VMS deposits: the so-called ultramafic-hosted VMS (UM-VMS) deposits (e.g. Outokumpu deposit; Patten et al. 2022).

The UM-VMS and UM-SMS deposits formed as a result of hydrothermal events in volcanic submarine environments are characterised by relatively high contents of critical element such as Co, Ni, Sn, as well as precious and base metals (Fouquet et al. 2010; Maslennikov et al. 2017; Toffolo et al. 2020; Choi et al. 2021; Patten et al. 2022). Among those critical elements, however, significant contents of Sn are unexplained in terms of modern seafloor hydrothermal mineralisation because the source of Sn in VMS deposits was thought to be related to highly evolved magmatism underlying oceanic crust and/or detrital sediments from continents (Bleeker and Hester 1999; Hannington et al. 1999; Serranti et al. 2002). In addition, sulfides of modern SMS deposits have similar but highly variable Sn abundances regardless of the submarine environment (Peltonen et al. 2008 and their references). However, most UM-SMS deposits at MOR settings show consistent and relatively high average concentrations of Sn (up to ~ 2000 ppm) as compared with mafic-hosted SMS deposits (Fouquet et al. 2010; Evrard et al. 2015; Choi et al. 2021), although the precipitation process of Sn into sulfides in UM-SMS deposits is still enigmatic.

Patten et al. (2022) showed relatively high abundance of critical elements including Sn in both UM-VMS and UM-SMS deposits. To better understand Sn mineralisation in SMS and VMS deposits, we plotted the Sn contents of pyrite and sphalerite in the Dergamysh and Buribay VMS deposits in the Urals. The pyrite and sphalerite have higher Sn contents in the Dergamysh deposit than in the Buribay deposit, where ancient chimneys show a genetical affinity with those from ultramafic- and MORB-hosted SMS deposits, respectively (Fig. 11; Maslennikov et al. 2017). The values are similar to those of MOR-related SMS deposits, suggesting that the contribution of different host rocks to the hydrothermal mineralisation is reflected in the distribution of Sn at the mineral scale. This suggests that trace element variations in sulfides from seafloor hydrothermal mineralisation may enhance our understanding of the source of metals in the UM-VMS deposits.

Sulfur source for hydrothermal mineralisation

The $\delta^{34}S$ values for pyrite from the different mineralisation stages exhibit a narrow range of 6.2 to 8.5‰, with a median value of 6.7‰ ($n = 10$; Table 3). These values can be explained by mixing between S of igneous origin (−2 to +2‰; Sakai et al. 1984; Alt et al. 1989, 2007; Alt and Anderson 1991) and S from the thermochemical sulfate reduction of seawater (+21‰; Rees et al. 1978) (Fig. 10). The proportions of S derived from these reservoirs can be calculated with the two end-member mixing model of Arnold and Sheppard (1981). We estimate that seawater sulfate is 29–40% of the S in the AVF pyrite (Table 3). This indicates that S was mainly derived from the associated igneous host rocks (60–70%), whereas a relatively smaller proportion of seawater S was incorporated into the AVF pyrite by fluid-seawater mixing. Therefore, we conclude that the AVF is a rock-dominated system and that the fluid–rock interaction (i.e. wall-rock leaching) during hydrothermal circulation is the dominant source of S and most metals. In particular, a comparison with other MOR systems shows that relatively high $\delta^{34}S$ values (> 10‰) are limited to ultramafic-hosted systems (e.g. Rainbow, Logatchev, and Tianzuo; Fig. 10). This is likely due to the long history of fluid–rock interactions and greater proportion of seawater sulfate when considering the long-lived, deep hydrothermal circulation compared to MORB-hosted systems (Knight et al. 2018; Tao et al. 2020).

Conclusions

Hydrothermal sulfides from ultramafic-hosted mineralisation were collected from the Ari vent field on the slow-spreading middle part of the Central Indian Ridge. The sulfide samples can be classified as Fe–Cu- and Cu-rich types based on the major sulfide minerals. The Fe–Cu-rich sulfide samples record three different mineralisation stages: (1) stage I (subhedral–euhedral pyrite + isocubanite ± chalcopyrite ± magnetite ± pyrrhotite); (2) stage II (colloform pyrite ± sphalerite ± galena ± electrum); and (3) stage III (chalcocite ± uraninite) dominated by seawater alteration. As the AVF mineralisation progressed from stages I to III, the fluid temperature and fS_2 decreased and fO_2 increased. The Cu-rich sulfide samples are characterised by mineral assemblages and a paragenesis similar to those of the Fe–Cu-rich sulfide samples, but the more Cu-rich mineralisation with a higher proportion of isocubanite is indicative of relatively high-temperature and reducing mineralisation conditions.

The U-rich (up to 51.9 ppm) and Sn-poor (up to 2.1 ppm) compositions of the AVF sulfide samples are different from those of other ultramafic-hosted SMS deposits. The predominant occurrence of uraninite (< 1 µm in size) on altered surfaces of pyrite and hematite is the main form of U enrichment in the AVF. Ambient seawater was likely the principal source of U, and subsequent oxidative alteration of Fe-bearing minerals may have had an important role in the fixation of seawater-derived U to precipitate the discrete uraninite.

A comparison of sulfide minerals in different types of hydrothermal vent fields at MOR spreading centres reveals that Sn contents vary systematically between MORB- and ultramafic-hosted sphalerite and pyrite, with much higher Sn concentrations in the ultramafic-hosted environments. Sphalerite is one of the major hosts of Sn, whereas pyrite is Sn-poor. Therefore, the lower Sn contents of the Fe–Cu-rich sulfide samples (average = 6.1 ppm Sn) as compared with the Cu-rich sulfide samples (average = 48.9 ppm Sn) in the AVF are most likely due to Fe-rich mineralisation. These results suggest that the geochemistry of sulfide minerals rather than the bulk chemical composition of hydrothermal samples provides a clearer understanding of the nature of hydrothermal mineralisation in MOR settings. Tin could be one of the most effective elements for investigating the ore-forming processes in ultramafic-hosted hydrothermal deposits at MOR settings. This is also evidenced by a comparison of ancient VMS deposits, showing that the Sn contents of pyrite and sphalerite are higher in UM-VMS deposit than in mafic-hosted VMS deposit.

In situ $\delta^{34}S$ values (+6.2 to +8.5‰) of pyrite indicate that the S was mainly derived from the host igneous rocks ($\delta^{34}S$ −2 to +2‰) with a smaller contribution (29–40%) of reduced seawater S ($\delta^{34}S$ +21‰). This indicates that fluid–rock interactions were significant in supplying the S and metals to the fluids in the AVF. Reducing, high-temperature fluids circulating through ultramafic rocks were important in forming the AVF. Such rock-dominated systems influenced by ultramafic-hosted mineralisation may be common along slow-spreading MOR settings.

Supplementary Information The online version contains supplementary material available at https://doi.org/10.1007/s00126-023-01191-x.

Acknowledgements The authors thank the scientists and crews of the R/V *ISABU* for their support during the sampling and data collection. Careful reviews by T. Nozaki and anonymous reviewers are greatly appreciated, as they improved the quality of this manuscript. The authors also thank chief editor G. Beaudoin and associate editor A. Cabral for valuable comments on the manuscript.

Funding This research was financially supported by the Ministry of Oceans and Fisheries of Korea (20210634), the Korea Institute of Ocean Science and Technology (PEA0124) and Korea Institute of Geoscience and Mineral Resources (GP2023-004).

Declarations

Conflict of interest The authors declare no competing interests.

References

Alt JC, Anderson TF (1991) Mineralogy and isotopic composition of sulfur in layer 3 gabbros from the Indian Ocean, Hole 735B. In Proc. Ocean Drill Program Sci Results 118:113–125

Alt JC, Anderson TF, Bonnell L (1989) The geochemistry of sulfur in a 1.3 km section of hydrothermally altered oceanic crust, DSDP Hole 504B. Geochim Cosmochim Acta 53:1011–1023

Alt JC, ShanksWC BW, Paulick H, Garrido CJ, Beaudoin G (2007) Hydrothermal alteration and microbial sulfate reduction in peridotite and gabbro exposed by detachment faulting at the Mid-Atlantic Ridge, 15° 20´ N (ODP Leg 209): a sulfur and oxygen isotope study. Geochem Geophys Geosyst 8(8):Q08002

Arnold M, Sheppard SMF (1981) East Pacific Rise at latitude 21°N: isotopic composition and origin of the hydrothermal sulphur. Earth Planet Sci Lett 56:148–156

Ayupova NR, Melekestseva IY, Maslennikov VV, Tseluyko AS, Blinov IA, Beltenev VE (2018) Uranium accumulation in modern and ancient Fe-oxide sediments: examples from the Ashadze-2 hydrothermal sulfide field (Mid-Atlantic Ridge) and Yubileynoe massive sulfide deposit (South Urals, Russia). Sediment Geol 367:164–174

Barrie CT, Hannington MD (1999) Classification of volcanic-associated massive sulfide deposits based on host-rock composition. Rev Econ Geol 8:1–12

Belousov I, Danyushevsky LV, Olin PH, Gilbert, S, Thompson, JM (2014) New calibration standard for LA–ICPMS analysis of sulphides. AGU, 2014 Fall Meeting. https://agu.confex.com/agu/fm14/webprogram/Paper19453.html

Bleeker W, Hester BW (1999) Discovery of the Kidd Creek massive sulphide ore body: a historical perspective. Econ Geol Monogr 10:31–42

Butler I, Nesbitt R (1999) Trace element distributions in the chalcopyrite wall of a black smoker chimney: insights from laser ablation inductively coupled plasma mass spectrometry (LA–ICP–MS). Earth Planet Sci Lett 167:335–345

Cao H, Sun Z, Zhai S, Cao Z, Jiang X, Huang W, Wang L, Zhang X, He Y (2018) Hydrothermal processes in the Edmond deposits, slow- to intermediate-spreading Central Indian Ridge. J Mar Syst 180:197–210

Cao H, Sun Z, Jiang Z, Dong A, Geng W, Zhang X, Li X, Yan D, Liu W (2021) Source origin and ore-controlling factors of hydrothermal sulfides from the Tianzuo hydrothermal field, Southwest Indian Ridge. Ore Geol Rev 134:104168

Charlou J, Donval J, Fouquet Y, Jean-Baptiste P, Holm N (2002) Geochemistry of high H_2 and CH_4 vent fluids issuing from ultramafic rocks at the Rainbow hydrothermal field (36°14′N, MAR). Chem Geol 191:345–359

Choi SK, Pak SJ, Kim J, Park J-W, Son S-K (2021) Gold and tin mineralisation in the ultramafic-hosted Cheoeum vent field, Central Indian Ridge. Miner Depos 56:885–906

Choi SK, Pak SJ, Park J-W, Kim HS, Kim J, Choi SH (2023) Trace-element distribution and ore-forming processes in Au–Ag-rich hydrothermal chimneys and mounds in the TA25 West vent field of the Tonga Arc. Miner Depos 58:135–160

Cook NJ, Ciobanu CL, Pring A, Skinner W, Shimizu M, Danyushevsky L, Saini-Eidukat B, Melcher F (2009) Trace and minor elements in sphalerite: a LA–ICPMS study. Geochim Cosmochim Acta 73:4761–4791

Corliss JB, Dymond J, Gordon LI, Edmond JM, von Herzen RP, Ballard RD, Green K, Williams D, Bainbridge A, Crane K, van Andel TH (1979) Submarine thermal springs on the Galápagos Rift. Science 203:1073–1083

Ding T, Tao C, Dias ÁA, Liang J, Chen J, Wu B, Ma D, Zhang R, Wang J, Liao S, Wang Y, Yang W, Liu J, Li W, Zhang G, Huang H (2021) Sulfur isotopic compositions of sulfides along the Southwest Indian Ridge: implications for mineralization in ultramafic rocks. Miner Depos 56:991–1006

Ding T, Wang J, Tao CH, Dias AA, Liang J, Wang Y, Chen J, Wu B, Huang H (2022) Trace-element compositions of sulfides from inactive Tianzuo hydrothermal field, Southwest Indian Ridge: implications for ultramafic rocks hosting mineralization. Ore Geol Rev 140:104421

Douville E, Charlou J, Oelkers E, Bienvenu P, Jove Colon C, Donval J, Fouquet Y, Prieur D, Appriou P (2002) The rainbow vent fluids (36°14′N, MAR): the influence of ultramafic rocks and phase separation on trace metal content in Mid-Atlantic Ridge hydrothermal fluids. Chem Geol 184:37–48

Escartín J, Smith DK, Cann J, Schouten H, Langmuir CH, Escrig S (2008) Central role of detachment faults in accretion of slow-spreading oceanic lithosphere. Nature 455:790–794

Evrard C, Fouquet Y, Moëlo Y, Rinnert E, Etoubleau J, Langlade JA (2015) Tin concentration in hydrothermal sulphides related to ultramafic rocks along the Mid-Atlantic Ridge: a mineralogical study. Eur J Mineral 27:627–638

Fouquet Y, von Stackelberg U, Charlou JL, Erzinger J, Herzig PM, Muehe R, Wiedicke M (1993) Metallogenesis in back-arc environments; the Lau Basin example. Econ Geol 88:2154–2181

Fouquet Y, Cambon P, Etoubleau J, Charlou JL, Ondréas H, Barriga FJAS, Cherkashov G, Semkova T, Poroshina I, Bohn M, Donval JP, Henry K, Murphy P, Rouxel O (2010) Geodiversity of hydrothermal processes along the Mid-Atlantic Ridge and ultramafic-hosted mineralization: a new type of oceanic Cu–Zn–Co–Au volcanogenic massive sulfide deposit. Diversity of hydrothermal systems on slow spreading ocean ridges. Geophys Monogr Ser 188:321–367

Fu J, Hu Z, Zhang W, Yang L, Liu Y, Li M, Zong K, Gao S, Hu S (2016) In situ sulfur isotopes ($\delta^{34}S$ and $\delta^{33}S$) analyses in sulfides and elemental sulfur using high sensitivity cones combined with the addition of nitrogen by laser ablation MC-ICPMS. Anal Chim Acta 911:14–26

Fuchs S, Hannington MD, Petersen S (2019) Divining gold in seafloor polymetallic massive sulfide systems. Miner Depos 54:789–820

George LL, Cook NJ, Ciobanu CL (2016) Partitioning of trace elements in co-crystallized sphalerite-galena-chalcopyrite hydrothermal ores. Ore Geol Rev 77:97–116

Graham UM, Bluth GJ, Ohmoto H (1988) Sulfide-sulfate chimneys on the East Pacific Rise, 11° and 13° N latitudes. Part 1: mineralogy and paragenesis. Can Mineral 26:487–504

Grant HLJ, Hannington MD, Petersen S, Frische M, Fuchs SH (2018) Constraints on the behavior of trace elements in the actively-forming TAG deposit, Mid-Atlantic Ridge, based on LA-ICP-MS analyses of pyrite. Chem Geol 498:45–71

Grundler PV, Brugger J, Etschmann BE, Helm L, Liu W, Spry PG, Tian Y, Testemale D, Pring A (2013) Speciation of aqueous tellurium(IV) in hydrothermal solutions and vapors, and the role of oxidized tellurium species in Te transport and gold deposition. Geochim Cosmochim Acta 120:298–325

Hannington MD, Herzig P, Scott S, Thompson G, Rona P (1991) Comparative mineralogy and geochemistry of gold-bearing sulfide deposits on the mid-ocean ridges. Mar Geol 101:217–248

Hannington MD, Bleeker W, Kjarsgaard I (1999) Sulfide mineralogy, geochemistry and ore genesis of the Kidd creek deposit: part I. North, central, and south orebodies. Econ Geol Monogr 10:163–224

Hannington MD, de Ronde CEJ, Petersen S (2005) Sea-floor tectonics and submarine hydrothermal systems. Econ Geol 100th Anniversary Volume, pp 111–141

Hannington MD, Jamieson J, Monecke T, Petersen S (2010) Modern sea-floor massive sulfides and base metal resources: toward an estimate of global sea-floor massive sulfide potential. Soc Econ Geol 15:317–338

Hannington MD, Jamieson J, Monecke T, Petersen S, Beaulieu S (2011) The abundance of seafloor massive sulfide deposits. Geology 39:1155–1158

Hegner E, Tatsumoto M (1989) Pb, Sr, and Nd isotopes in seamount basalts from the Juan de Fuca Ridge and Kodiak-Bowie Seamount Chain, northeast Pacific. J Geophys Res 94:17839

Huston DL, Sie SH, Suter GF, Cooke DR, Both RA (1995) Trace elements in sulfide minerals from eastern Australian volcanic-hosted massive sulfide deposits: part I. Proton microprobe analyses of pyrite, chalcopyrite, and sphalerite, and part II. Selenium levels in pyrite: comparison with $\delta^{34}S$ values and implications for the source of sulfur in volcanogenic hydrothermal systems. Econ Geol 90:1167–1196

Hutchison MN, Scott SD (1981) Sphalerite geobarometry in the Cu–Fe–Zn–S system. Econ Geol 76:143–153

Kawasumi S, Chiba H (2017) Redox state of seafloor hydrothermal fluids and its effect on sulfide mineralization. Chem Geol 451:25–37

Keith M, Haase KM, Schwarz-Schampera U, Klemd R, Petersen S, Bach W (2014) Effects of temperature, sulfur, and oxygen fugacity on the composition of sphalerite from submarine hydrothermal vents. Geology 42:699–702

Keith M, Häckel F, Haase KM, Schwarz-Schampera U, Klemd R (2016) Trace element systematics of pyrite from submarine hydrothermal vents. Ore Geol Rev 72:728–745

Kim J, Son S, Kim D, Pak S, Yu OH, Walker SL, Oh J, Choi SK, Ra K, Ko Y, Kim K, Lee J, Son J (2020) Discovery of active hydrothermal vent fields along the Central Indian Ridge, 8–12°S. Geochem Geophys Geosystems 21:1–21

Knight DR, Roberts S, Webber A (2018) The influence of spreading rate, basement composition, fluid chemistry and chimney morphology on the formation of gold-rich SMS deposits at slow and ultraslow mid-ocean ridges. Miner Depos 53:143–152

Li R, Chen H, Xia X, Yang Q, Li L, Xu J, Huang C, Danyushevsky LV (2017) Ore fluid evolution in the giant Marcona Fe–(Cu) deposit, Perú: evidence from in-situ sulfur isotope and trace element geochemistry of sulfides. Ore Geol Rev 86:624–638

Liao SL, Tao CH, Li HM, Barriga FJAS, Liang J, Yang WF, Yu JY, Zhu GW (2018) Bulk geochemistry, sulfur isotope characteristics of the Yuhuang-1 hydrothermal field on the ultraslow-spreading Southwest Indian Ridge. Ore Geol Rev 96:13–27

Liao S, Zhu C, Zhou J, Liu W, Yu J, Liang J, Yang W, Li W, Liu J, Tao C (2021) Distal axis sulfide mineralization on the ultraslow-spreading Southwest Indian Ridge: an LA-ICP-MS study of pyrite from the East Longjing-2 hydrothermal field. Acta Oceanol Sin 40(5):105–113

Longerich HP, Jackson SE, Günther D (1996) Laser ablation inductively coupled plasma mass spectrometric transient signal data acquisition and analyte concentration calculation. J Anal at Spectrom 11:899–904

Lusk J, Bray DM (2002) Phase relations and the electrochemical determination of sulfur fugacity for selected reactions in the Cu–Fe–S and Fe–S systems at 1 bar and temperatures between 185 and 460 °C. Chem Geol 192:227–248

Martin AJ, McDonald I, Jenkin GRT, McFall KA, Boyce AJ, Jamieson JW, MacLeod CJ (2021) A missing link between ancient and active mafic-hosted seafloor hydrothermal systems – magmatic volatile influx in the exceptionally preserved Mala VMS deposit, Troodos. Cyprus Chem Geol 567:120127

Marques AFA, Barriga F, Chavagnac V, Fouquet Y (2006) Mineralogy, geochemistry, and Nd isotope composition of the Rainbow hydrothermal field, Mid-Atlantic Ridge. Miner Depos 41:52–67

Maslennikov VV, Maslennikova SP, Large RR, Danyushevsky LV (2009) Study of trace element zonation in vent chimneys from the Silurian Yaman-Kasy volcanic-hosted massive sulfide deposit (Southern Urals, Russia) using laser ablation–inductively coupled plasma mass spectrometry (LA–ICPMS). Econ Geol 104:1111–1141

Maslennikov VV, Ayupova NR, Herrington RJ, Danyushevskiy LV, Large RR (2012) Ferruginous and manganiferous haloes around massive sulphide deposits of the Urals. Ore Geol Rev 47:5–41

Maslennikov VV, Maslennikova SP, Large RR, Danyushevsky LV, Herrington RJ, Ayupova NR, Zaykov VV, Lein AY, Tseluyko AS, Melekestseva IY, Tessalina SG (2017) Chimneys in Paleozoic massive sulfide mounds of the Urals VMS deposits: mineral and trace element comparison with modern black, grey, white and clear smokers. Ore Geol Rev 85:64–106

Maslennikov VV, Cherkashov G, Artemyev DA, Firstova A, Large RR, Tseluyko A, Kotlyarov V (2020) Pyrite varieties at Pobeda hydrothermal fields, Mid-Atlantic Ridge 17°07’–17°08’ N: LAICP-MS data deciphering. Mineral 10:622

McCaig AM, Cliff RA, Escartin J, Fallick AE, MacLeod CJ (2007) Oceanic detachment faults focus very large volumes of black smoker fluids. Geology 35:935

Melekestseva IY, Tret’yakov GA, Nimis P, Yuminov AM, Maslennikov VV, Maslennikova SP, Kotlyarov VA, Beltenev VE, Danyushevsky LV, Large R (2014) Barite-rich massive sulfides from the Semenov-1 hydrothermal field (Mid-Atlantic Ridge, 13°30.87′ N): evidence for phase separation and magmatic input. Mar Geol 349:37–54

Melekestseva I, Maslennikov VV, Safina NP, Nimis P, Maslennikova S, Beltenev V, Rozhdestvenskaya I, Danyushevsky L, Large R, Artemyev D, Kotlyarov V, Toffolo L (2018) Sulfide breccias from the Semenov-3 hydrothermal field, Mid-Atlantic Ridge: authigenic mineral formation and trace element pattern. Minerals 8(8):321

Melekestseva IY, Maslennikov VV, Ayupova NR, Belogub EV, Maslennikova SP, Bel’tenev VE, Danyushevsky L, Large R (2020) Behavior of trace elements during oxidation of sphalerite of the Irinovskoe hydrothermal sulfide field (13°20′ N, Mid-Atlantic Ridge). Geol Ore Depos 62:254–259

Melekestseva I, Maslennikov V, Tret’yakov G, Maslennikova S, Danyushevsky L, Kotlyarov V, Large R, Beltenev V, Khvorov P (2020) Trace element geochemistry of sulfides from the Ashadze-2 hydrothermal field (12°58′ N, Mid-Atlantic Ridge): influence of host rocks, formation conditions or seawater? Minerals 10:1–29

Meng X, Li X, Chu F, Zhu J, Lei J, Li Z, Wang H, Chen L, Zhu Z (2020) Trace element and sulfur isotope compositions for pyrite across the mineralization zones of a sulfide chimney from the East Pacific Rise (1–2°S). Ore Geol Rev 116:103209

Metz S, Trefry JH (2000) Chemical and mineralogical influences on concentrations of trace metals in hydrothermal fluids. Geochim Cosmochim Acta 64:2267–2279

Migdisov AA, Williams-Jones AE (2005) An experimental study of cassiterite solubility in HCl-bearing water vapour at temperatures up to 350 °C: implications for tin ore formation. Chem Geol 217:29–40

Mills RA, Thomson J, Elderfield H, Hinton RW, Hyslop E (1994) Uranium enrichment in metalliferous sediments from the Mid-Atlantic Ridge. Earth Planet Sci Lett 124:35–47

Nakamura K, Morishita T, Bach W, Klein F, Hara K, Okino K, Takai K, Kumagai H (2009) Serpentinized troctolites exposed near the Kairei Hydrothermal Field, Central Indian Ridge: insights into the origin of the Kairei hydrothermal fluid supporting a unique microbial ecosystem. Earth Planet Sci Lett 280:128–136

Nakamura K, Watanabe H, Miyazaki J, Takai K, Kawagucci S, Noguchi T, Nemoto S, Watsuji T, Matsuzaki T, Shibuya T, Okamura K, Mochizuki M, Orihashi Y, Ura T, Asada A, Marie D, Koonjul M, Singh M, Beedessee G, Bhikajee M, Tamaki K (2012) Discovery of new hydrothermal activity and chemosynthetic fauna on the Central Indian Ridge at 18°–20°S. PLoS ONE 7:e32965

Pak SJ, Moon JW, Kim J, Chandler MT, Kim HS, Son J, Son SK, Choi SK, Baker ET (2017) Widespread tectonic extension at the Central Indian Ridge between 8°S and 18°S. Gondwana Res 45:163–179

Paton C, Hellstrom J, Paul B, Woodhead J, Hergt J (2011) Iolite: freeware for the visualisation and processing of mass spectrometric data. J Anal at Spectrom 26:2508–2518

Patten CGC, Pitcairn IK, Teagle DAH, Harris M (2016) Sulphide mineral evolution and metal mobility during alteration of the oceanic crust: Insights from ODP Hole 1256D. Geochim Cosmochim Acta 193:132–159

Patten CGC, Coltat R, Junge M, Peillod A, Ulrich M, Manatschal G, Kolb J (2022) Ultramafic-hosted volcanogenic massive sulfide deposits: an overlooked sub-class of VMS deposit forming in complex tectonic environments. Earth-Science Rev 224:103891

Peltonen P, Kontinen A, Huhma H, Kuronen U (2008) Outokumpu revisited: new mineral deposit model for the mantle peridotite-associated Cu–Co–Zn–Ni–Ag–Au sulphide deposits. Ore Geol Rev 33:559–617

Rees CE, JenkinsWJ MJ (1978) The sulphur isotope geochemistry of ocean water sulphate. Geochim Cosmochim Acta 42:377–382

Ren Y, Wohlgemuth-Ueberwasser CC, Huang F, Shi X, Li B, Oelze M, Schreiber A, Wirth R (2021) Distribution of trace elements in sulfides from Deyin hydrothermal field, Mid-Atlantic Ridge – implications for its mineralizing processes. Ore Geol Rev 128:103911

Sakai H, Des Marais DJ, Ueda A, Moore JG (1984) Concentrations and isotope ratios of carbon, nitrogen, and sulfur in ocean-floor basalts. Geochim Cosmochim Acta 48:2433–2442Schmidt K, Garbe-Schönberg D, Koschinsky A, Strauss H, Jost CL, Klevenz V, Königer P (2011) Fluid elemental and stable isotope composition of the Nibelungen hydrothermal field (8°18’S, Mid-Atlantic Ridge): constraints on fluid–rock interaction in heterogeneous lithosphere. Chem Geol 280:1–18

Schmidt K, Garbe-Schönberg D, Koschinsky A, Strauss H, Jost CL, Klevenz V, Königer P (2011) Fluid elemental and stable isotope composition of the Nibelungen hydrothermal field (8°18′S, Mid-Atlantic Ridge): constraints on fluid–rock interaction in heterogeneous lithosphere. Chem Geol 280:1–18

Scott SD, Barnes HL (1971) Sphalerite geothermometry and geobarometry. Econ Geol 66:653–669

Serranti S, Ferrini V, Umberto M, Cabri LJ (2002) Trace-element distribution in cassiterite and sulfides from rubané and massive ores of the Corvo deposit, Portugal. Can Mineral 40:815–835

Son J, Pak S-J, Kim J, Baker ET, You O-R, Son S, Moon J (2014) Tectonic and magmatic control of hydrothermal activity along the slow-spreading Central Indian Ridge, 8°S–17°S. Geochem Geophys Geosystems 15:2011–2020

Tao C, Seyfried WE, Lowell RP, Liu Y, Liang J, Guo Z, Ding K, Zhang H, Liu J, Qiu L, Egorov I, Liao S, Zhao M, Zhou J, Deng X, Li H, Wang H, Cai W, Zhang G, Zhou H, Lin J, Li W (2020) Deep high-temperature hydrothermal circulation in a detachment faulting system on the ultra-slow spreading ridge. Nat Commun 11(1):1–9

Toffolo L, Nimis P, Tret’yakov GA, Melekestseva IY, Beltenev VE (2020) Seafloor massive sulfides from mid-ocean ridges: exploring the causes of their geochemical variability with multivariate analysis. Earth-Science Rev 201:102958

Uchida E, Sakamori T, Matsunaga J (2002) Aqueous speciation of lead and tin chlorides in supercritical hydrothermal solutions. Geochem J 36:61–72

Wang Y, Han X, Petersen S, Jin X, Qiu Z, Zhu J (2014) Mineralogy and geochemistry of hydrothermal precipitates from Kairei hydrothermal field, Central Indian Ridge. Mar Geol 354:69–80

Wang Y, Han X, Petersen S, Frische M, Qiu Z, Huaiming L, Honglin L, Wu Z, Cui R (2017) Mineralogy and trace element geochemistry of sulfide minerals from the Wocan Hydrothermal Field on the slow-spreading Carlsberg Ridge, Indian Ocean. Ore Geol Rev 84:1–19

Wang Y, Han X, Petersen S, Frische M, Qiu Z, Cai Y, Zhou P (2018) Trace metal distribution in sulfide minerals from ultramafic-hosted hydrothermal systems: examples from the Kairei Vent Field, Central Indian Ridge. Minerals 8:526

Wilson SA, Ridley WI, Koenig AE (2002) Development of sulfide calibration standards for the laser ablation inductively coupled plasma mass spectrometry technique. J Anal at Spectrom 17:406–409

Ye L, Cook NJ, Ciobanu CL, Yuping L, Qian Z, Tiegeng L, Wei G, Yulong Y, Danyushevskiy L (2011) Trace and minor elements in sphalerite from base metal deposits in South China: A LA–ICPMS study. Ore Geol Rev 39:188–217

Yi SB, Oh CW, Pak SJ, Kim J, Moon JW (2014) Geochemistry and petrogenesis of mafic-ultramafic rocks from the Central Indian Ridge, latitude 8°-17° S: denudation of mantle harzburgites and gabbroic rocks and compositional variation of basalts. Int Geol Rev 56:1691–1719

Yuan B, Yu HJ, YangYM ZYX, Yang JC, Xu Y, Lin Z (2018) Zone refinement related to the mineralization process as evidenced by mineralogy and element geochemistry in a chimney fragment from the Southwest Indian Ridge at 49.6° E. Chem Geol 482:46–60

Zeng ZG, Ma Y, Chen S, Selby D, Wang XY, Yin XB (2017) Sulfur and lead isotopic compositions of massive sulfides from deep-sea hydrothermal systems: implications for ore genesis and fluid circulation. Ore Geol Rev 87:155–171

Authors and Affiliations

Sun Ki Choi[1] · Sang Joon Pak[1,2] · Jonguk Kim[1] · Ji Young Shin[3] · Seungjin Yang[1] · Hwimin Jang[4] · Seung-Kyu Son[1]

[1] Ocean Georesources Research Department, Korea Institute of Ocean Science and Technology, Busan, South Korea

[2] Present Address: Critical Minerals Research Center, Korea Institute of Geoscience and Mineral Resources, Daejeon, South Korea

[3] Laboratory of Orogenic Belts and Crustal Evolution, School of Earth and Space Sciences, Peking University, Beijing, China

[4] Vessel Operation & Observation Team, Korea Institute of Ocean Science and Technology, Geoje, South Korea